

# Minutes-long soft X-ray prompt emission from a compact object merger

An Li<sup>1,2†</sup>, Chen-Wei Wang<sup>3,4†</sup>, Niccolò Passaleva<sup>5,6†</sup>, Jie An<sup>4,7†</sup>,  
 Bin-Bin Zhang<sup>8,9\*</sup>, Eleonora Troja<sup>6,10\*</sup>, Yi-Han Iris Yin<sup>11,12\*</sup>,  
 Yuan Liu<sup>7</sup>, Shao-Lin Xiong<sup>3</sup>, Li-Ping Xin<sup>7</sup>, Yi-Xuan Shao<sup>8,9</sup>, Jun Yang<sup>13</sup>, Hui Sun<sup>7</sup>,  
 Dong Xu<sup>7</sup>, Yu-Han Yang<sup>6</sup>, Roberto Ricci<sup>6,14</sup>, He Gao<sup>1,2</sup>, Sarah Antier<sup>15</sup>,  
 Rosa L. Becerra<sup>6,16</sup>, Jia-Xin Cao<sup>17</sup>, Alberto Javier Castro-Tirado<sup>18</sup>, Xin-Lei Chen<sup>19</sup>,  
 Ye-Hao Cheng<sup>19</sup>, Yong Chen<sup>3</sup>, Hua-Qing Cheng<sup>7</sup>, Valerio D'Elia<sup>20</sup>,  
 Massimiliano De Pasquale<sup>21</sup>, Yong-Wei Dong<sup>3</sup>, Eslam Elhosseiny<sup>22</sup>,  
 Rob A. J. Eyles-Ferris<sup>23</sup>, Maria Gritsevich<sup>24,25</sup>, Xu-Hui Han<sup>7</sup>, Dieter Hartmann<sup>26</sup>,  
 You-Dong Hu<sup>17</sup>, Jing-Wei Hu<sup>7\*</sup>, Shu-Mei Jia<sup>3</sup>, Nino Kochiashvili<sup>27</sup>,  
 Wei-Hua Lei<sup>28</sup>, Andrew J. Levan<sup>29,30</sup>, Cheng-Kui Li<sup>3</sup>, Dong-Yue Li<sup>7</sup>, Hua-Li Li<sup>7\*</sup>,  
 Xiao-Bo Li<sup>3</sup>, Zhi-Xing Ling<sup>4,7</sup>, He-Yang Liu<sup>7</sup>, Hou-Jun Lü<sup>17</sup>, Daniele B. Malesani<sup>31,32,29</sup>,  
 Brendan O'Connor<sup>33</sup>, Hai-Wu Pan<sup>7</sup>, Shashi Bhushan Pandey<sup>34</sup>, Ignacio Perez-Garcia<sup>35</sup>,  
 Daniëlle L. A. Pieterse<sup>29</sup>, Marion Pillas<sup>36</sup>, Yu-Lei Qiu<sup>7</sup>, Andrea Saccardi<sup>37</sup>,  
 Rubén Sánchez-Ramírez<sup>38</sup>, Wen-Jun Tan<sup>3,4</sup>, Manasanun Tanasan<sup>39</sup>, Nial R. Tanvir<sup>23</sup>,  
 Susanna D. Vergani<sup>40</sup>, Jing Wang<sup>7</sup>, Xiao-Feng Wang<sup>41</sup>, Qin-Yu Wu<sup>4,7</sup>, Shu-Xu Yi<sup>3</sup>,  
 Tillayev Yusufjon<sup>42,43</sup>, Chen Zhang<sup>7</sup>, Wen-Da Zhang<sup>7</sup>, Yi-Jia Zhang<sup>41</sup>, Guo-Ying Zhao<sup>44</sup>,  
 Chao Zheng<sup>3</sup>, Shi-Jie Zheng<sup>3</sup>, Chang Zhou<sup>28</sup>, Ping Zhou<sup>8</sup>, Bertrand Cordier<sup>45</sup>,  
 Jian-Yan Wei<sup>7</sup>, Weimin Yuan<sup>4,7</sup>, Shuang-Nan Zhang<sup>3,4</sup>, Bing Zhang<sup>11,12,46</sup>

<sup>1</sup>School of Physics and Astronomy, Beijing Normal University, Beijing 100875, China

<sup>2</sup>Institute for Frontier in Astronomy and Astrophysics, Beijing Normal University, Beijing 102206, China

<sup>3</sup>State Key Laboratory of Particle Astrophysics, Institute of High Energy Physics,  
Chinese Academy of Sciences, Beijing 100049, China

<sup>4</sup>University of Chinese Academy of Sciences, Chinese Academy of Sciences, Beijing 100049, China

<sup>5</sup>Department of Physics, University of Rome, "Sapienza", Rome, Italy

<sup>6</sup>Department of Physics, University of Rome "Tor Vergata", Rome, Italy

<sup>7</sup>National Astronomical Observatories, Chinese Academy of Sciences, Beijing 100101, China

<sup>8</sup>School of Astronomy and Space Science, Nanjing University, 163 Xianlin Avenue, Nanjing 210023, China

<sup>9</sup>Key Laboratory of Modern Astronomy and Astrophysics, Nanjing University,  
Ministry of Education, Nanjing 210023, China

<sup>10</sup>INAF, Istituto di Astrofisica e Planetologia Spaziali, Rome, Italy

<sup>11</sup>The Hong Kong Institute for Astronomy and Astrophysics, The University of Hong Kong, Hong Kong, China

<sup>12</sup>Department of Physics, The University of Hong Kong, Pokfulam Road, Hong Kong, China

<sup>13</sup>Institute for Astrophysics, School of Physics, Zhengzhou University, Zhengzhou 450001, China

<sup>14</sup>INAF, Istituto di Radioastronomia, Bologna, Italy

<sup>15</sup>IJCLab, Univ Paris-Saclay, CNRS/IN2P3, Orsay, France

<sup>16</sup>Instituto de Astronomía, Universidad Nacional Autónoma de México, Ciudad de México, México

<sup>17</sup>Guangxi Key Laboratory for Relativistic Astrophysics, Department of Physics, Guangxi University,  
Nanning 530004, China

<sup>18</sup>Instituto de Astrofísica de Andalucía (IAA-CSIC), Glorieta de la Astronomía s/n, E-18008, Granada, Spain

<sup>19</sup>School of Physics and Astronomy, Yunnan University, 650500, Kunming, China

<sup>20</sup>Space Science Data Center (SSDC) - Agenzia Spaziale Italiana (ASI), Via del Politecnico snc,  
00133 Roma, Italy

<sup>21</sup>Department of Mathematics and Computer Sciences, Physical Sciences and Earth Sciences of University of Messina,

Via F.S. D'Alcontres 31, 98166 Messina, Italy

<sup>22</sup>National Research Institute of Astronomy and Geophysics (NRIAG), 1 El-marsad St., 11421 Helwan, Cairo, Egypt

<sup>23</sup>School of Physics and Astronomy, University of Leicester, University Road, Leicester, LE1 7RH, UK

<sup>24</sup>Faculty of Science, University of Helsinki, Gustaf Hallströmin katu 2, FI-00014 Helsinki, Finland

<sup>25</sup>Institute of Physics and Technology, Ural Federal University, Mira str. 19, 620002 Ekaterinburg, Russia

<sup>26</sup>Clemson University, Department of Physics and Astronomy, Clemson, SC 29634-0978, USA

<sup>27</sup>E. Kharadze Georgian National Astrophysical Observatory, Mt. Kanobili, Abastumani, 0301 Adigeni, Georgia

<sup>28</sup>Department of Astronomy, School of Physics,

Huazhong University of Science and Technology, Wuhan 430074, China

<sup>29</sup>Department of Astrophysics/IMAPP, Radboud University Nijmegen, P.O. Box 9010,

Nijmegen, 6500 GL, The Netherlands

<sup>30</sup>Department of Physics, University of Warwick, Coventry, CV4 7AL, UK

<sup>31</sup>Cosmic Dawn Center (DAWN), Denmark

<sup>32</sup>Niels Bohr Institute, University of Copenhagen, Jagtvej 155, 2200 Copenhagen N, Denmark

<sup>33</sup>McWilliams Center for Cosmology and Astrophysics, Department of Physics, Carnegie Mellon University,

Pittsburgh, PA, USA

<sup>34</sup>Aryabhatta Research Institute of Observational Sciences (ARIES), Manora Peak, Nainital, Uttarakhand, India, 263001

<sup>35</sup>Instituto de Astrofísica de Andalucía (IAA-CSIC), Granada, Spain

<sup>36</sup>Sorbonne Université, CNRS, UMR 7095, Institut d'Astrophysique de Paris,

98 bis boulevard Arago, 75014 Paris, France

<sup>37</sup>Université Paris-Saclay, Université Paris Cité, CEA, CNRS, AIM, 91191, Gif-sur-Yvette, France

<sup>38</sup>Instituto de Astrofísica de Andalucía, Consejo Superior de Investigaciones Científicas (IAA-CSIC),

Glorieta de la Astronomía, s/n, 18080, Granada, Spain

<sup>39</sup>National Astronomical Research Institute of Thailand (NARIT), Chiang Mai 50180, Thailand

<sup>40</sup>LUX, Observatoire de Paris, Université PSL, CNRS, Sorbonne Université, Meudon, 92190, France

<sup>41</sup>Department of Physics, Tsinghua University, Beijing, 100084, China

<sup>42</sup>Ulugh Beg Astronomical Institute, Uzbekistan Academy of Sciences, Astronomy St. 33, Tashkent 100052, Uzbekistan

<sup>43</sup>National University of Uzbekistan, University Str. 4, Tashkent 100174, Uzbekistan

<sup>44</sup>School of Physics and Astronomy, Sun Yat-Sen University, Zhuhai, 519082, China

<sup>45</sup>CEA Paris-Saclay, Irfu/Département d'Astrophysique, 9111 Gif sur Yvette, France

<sup>46</sup>Nevada Center for Astrophysics and Department of Physics and Astronomy, University of Nevada, Las Vegas,

NV 89154, USA

\*Corresponding author. Email: B.-B. Z. (bbzhang@nju.edu.cn), E. T. (eleonora.troja@uniroma2.it), Y.-H. I. Y. (iris.yh.yin@connect.hku.hk), J.-W. H. (hujingwei@nao.cas.cn), H.-L. L. (lhl@nao.cas.cn)

<sup>†</sup>These authors contributed equally to this work.

**Compact object mergers are multi-messenger sources and progenitors of some gamma-ray bursts (GRBs), primarily understood by gamma-ray observations, while poorly constrained in the prompt low-energy phase. A long-lasting X-ray emission was discussed as afterglows following several short-duration ( $\lesssim 2$  s) bursts, yet this prompt X-ray component was not directly observed or confirmed. Here we report the discovery of a minutes-long ( $\sim 560$  s) flash of soft X-rays immediately following the short ( $\sim 0.4$  s) GRB 250704B. The long-soft bump points to a distinct phase of prompt emission in X-rays detected by Einstein Probe in an event that otherwise appear as an ordinary short GRB, showing that long-lasting X-ray emission is likely a common feature of merger-driven bursts and a promising electromagnetic counterpart to gravitational-wave sources.**

**One sentence summary:** Einstein Probe detected a long-soft X-ray counterpart exhibiting variability and spectral evolution as a distinct phase of prompt emission accompanying a short GRB, pointing to long-lasting X-ray emission as a potentially common feature of merger-driven bursts and a promising electromagnetic counterpart to gravitational-wave sources.

Mergers of compact objects containing neutron stars are among the most energetic events in the Universe, forming a central engine that drives relativistic outflows and powers gamma-ray bursts (GRBs) (1–3). While canonical GRBs have been studied primarily through their gamma-ray emission, an emerging population of extragalactic fast X-ray transients (EFXTs) has hinted at additional high-energy phases (4–7). Notably, two EFXTs detected by Chandra—CDF-S XT1 and XT2—have been interpreted as possible magnetar-powered X-ray emission following binary neutron star mergers (8, 9), and although subsequent JWST observations refined their redshifts, host-galaxy properties, and energetics, their physical origin remains unsettled (10). An X-ray counterpart to GRB 050709 reported by HETE displayed a long-soft component after the short spike, which was claimed to be the onset of afterglow given its smooth temporal profile and lack of spectral evolution (11). Even with these rare cases, X-ray counterpart detection that begins at the burst onset and extends over long durations has remained exceedingly rare, yet is crucial for directly probing central-engine activity, especially in merger-driven short GRBs.

## Observations of EP250704a/GRB 250704B

EP250704a is a long-lasting X-ray transient discovered in the 0.5–4 keV band by the Wide-field X-ray Telescope (WXT) onboard the *Einstein Probe* (EP) mission (12). It is detected starting at  $\sim T_0 + 0.2$  s (13), where  $T_0 = 08:16:27.10$  UTC on 2025 July 4 denotes the trigger time of GRB 250704B, a short duration ( $T_{90} = 0.37 \pm 0.06$  s) GRB independently discovered by *Space Variable Objects Monitor (SVOM)*/Gamma-ray Burst Monitor (GRM) (14), *Insight-HXMT* (15), and *Konus-Wind* (16) (Methods). The WXT light curve of EP250704a, shown in Fig. 1, comprises three episodes separated by periods of apparent quiescence: an initial sharp spike (Episode I) beginning at  $T_0 + 0.25$  s with a total duration of  $T_{90,X} = 0.35^{+0.01}_{-0.05}$  s (Fig. 2b); a seconds-long tail (Episode II), followed by a temporally extended X-ray bump (Episode III) of  $\sim 540$  s starting at  $\sim T_0 + 20$  s. The initial spike of EP250704a is temporally and spatially coincident with the brightest pulse of GRB 250704B, unambiguously tying these two high-energy transients to a common origin. However, their temporal profiles are drastically different: whereas EP250704a displays a long-lasting multi-episode prompt X-ray emission (Episode II and Episode III), no gamma-rays are detected during this phase down to  $2.13 \times 10^{-9}$  erg cm $^{-2}$  s $^{-1}$  in the 15–150 keV energy range

(Fig. 1e).

### Association with compact-binary merger

Emission from EP250704a triggered WXT at  $\sim T_0 + 25$  s, initiating an automatic slew with the Follow-up X-ray Telescope (FXT) (17). Starting at  $\sim T_0 + 227$  s, FXT observations localized a fading X-ray afterglow (Fig. 1a, b). Subsequent optical and radio follow-up identified counterparts and established a redshift of  $z = 0.66102 \pm 0.00011$  (see Methods). At this distance, the prompt gamma-ray spectrum of GRB 250704B/EP250704a peaks at  $E_{\text{peak},z} = 978^{+153}_{-203}$  keV (rest-frame) and the isotropic-equivalent energy released in the 10–1000 keV band is  $E_{\text{iso}} = 3.79^{+0.20}_{-0.25} \times 10^{51}$  erg. These values place the burst well outside the population of GRBs from collapsing massive stars (18) (collapsars; Type II) and within the population of merger-driven GRBs (Type I; Extended Data Fig. S4). At  $z \sim 0.661$ , the distinctive signals of a merger-driven explosion, either a gravitational wave chirp or an optical/infrared kilonova, are beyond the reach of current ground-based facilities. Nonetheless, our deep optical limits (Fig. 5) rule out a bright supernova (19, 20), making a collapsar origin unlikely. Therefore, beyond the short GRB duration itself, standard optical and gamma-ray constraints strengthen the association between EP250704a/GRB 250704B and a compact-binary merger.

### Unique high-energy properties

The properties of EP250704a itself distinguish it from the larger population of extragalactic fast X-ray transients (EFXTs). Although multiple-episode behavior is seen in some EFXTs, the presence of a short, well-defined leading spike (Episode I) in EP250704a is unprecedented among EFXTs detected by EP (Fig. 2e). A Bayesian-block analysis of this feature yields a minimum variability timescale (MVT) of  $\sim 38$  ms, an outlier relative to the EP sample (Fig. 2c). On the MVT– $T_{90}$  diagram, both the initial X-ray spike of EP250704a and the gamma-ray emission of GRB 250704B fall within the region of Type I bursts (Fig. 2d). Consistently with this result, we find that the sharp X-ray spike (Episode I) in EP250704a is morphologically and spectrally tied to the bright, second gamma-ray pulse in the short GRB 250704B (Fig. 3; Methods), and can be interpreted as its low-energy extension. In this context, the delayed X-ray onset arises naturally from the compactness and baryon loading of the emitting region during the initial gamma-ray pulse: self-absorption suppresses

the low-energy spectrum early on (21), but as the jet excavates a low-density funnel through the merger ejecta, later prompt episodes reach larger radii and emerge in X-rays (22) (Methods).

## Internal origin of the X-ray component

A connection between compact binary mergers and long duration EFXTs has already been proposed (8, 9, 23), but never definitively confirmed (10). In an earlier example, a long-soft X-ray component was detected in the short GRB 050709. However it was interpreted as standard afterglow onset owing to its smoothness and lack of spectral evolution (11). In EP250704a, by contrast, multi-epoch, broadband coverage reveals clear signatures of ongoing central-engine activity, providing the missing link between some EFXTs and their merger progenitors. Three observational facts point to an internal, engine-powered origin for the temporally extended X-ray component up to  $\sim T_0 + 400$  s: (i) rapid variability with  $\Delta t/t \lesssim 0.1$ , incompatible with a forward-shock afterglow (24, 25); (ii) a subsequent spectral hardening (Extended Data Fig. S3; Methods)—robust whether absorption is fixed or free—marking the transition from prompt to afterglow emission (26); and (iii) temporal and spectral indices comparable to early X-ray light curves of short GRBs (Fig. 4) attributed to internal plateaus (27). Additionally, a long-lived central engine is supported by the afterglow evolution at later times. The shallow X-ray decay from  $T_0 + 690$  s to  $7.2 \times 10^4$  s together with the slow optical rise from  $T_0 + 2 \times 10^3$  s to  $6.5 \times 10^4$  s require sustained energy injection, naturally provided by a long-lived magnetar central engine (Fig. 5; Methods). Therefore, we attribute the extended X-ray bump (Episode III) to long-lasting, engine-powered emission, indicating that the merger remnant—most likely a long-lived magnetar—remained active well beyond the gamma-ray phase.

## Conclusions and implications

Historically, long-lasting prompt emission in merger-driven bursts has been identified only in a minority ( $\simeq 10\text{--}15\%$ ) of cases — short GRBs with extended emission (28, 29) and rare long GRBs with hybrid properties (30–33). By revealing an X-ray bump in GRB 250704B, EP observations shift this paradigm. EP250704a demonstrates that a merger-driven burst can look like an ordinary short duration GRB in gamma-rays while exhibiting minutes-long emission in soft X-rays. The presence of X-ray plateaus was indirectly inferred by catching their final decaying tails (27, 34)

with the *Neil Gehrels Swift Observatory*, however, their onset, temporal profile and short-term variability were not observed due to the slew time gap.

Extrapolating the average flux of the soft X-ray bump to the 15–150 keV band places it below the detection threshold of the Burst Alert Telescope (BAT (35)) aboard the *Swift*. Therefore, had EP250704a been monitored solely in gamma-rays, only the 0.4-s spike would have been detected. This is not merely a tip-of-the iceberg effect caused by the burst’s distance scale. Detectability with *Swift*/BAT becomes feasible at  $z \lesssim 0.08$ , and even then the X-ray bump would be at best marginally visible near the  $\sim 10^{-8}$  erg cm $^{-2}$  s $^{-1}$  threshold (35). This is not the typical distance scale of short GRBs, localized by *Swift* at  $z \gtrsim 0.1$  (36). A long-lasting prompt X-ray component might therefore be prevalent in the sample of cosmological short GRBs, remaining undetected in most cases.

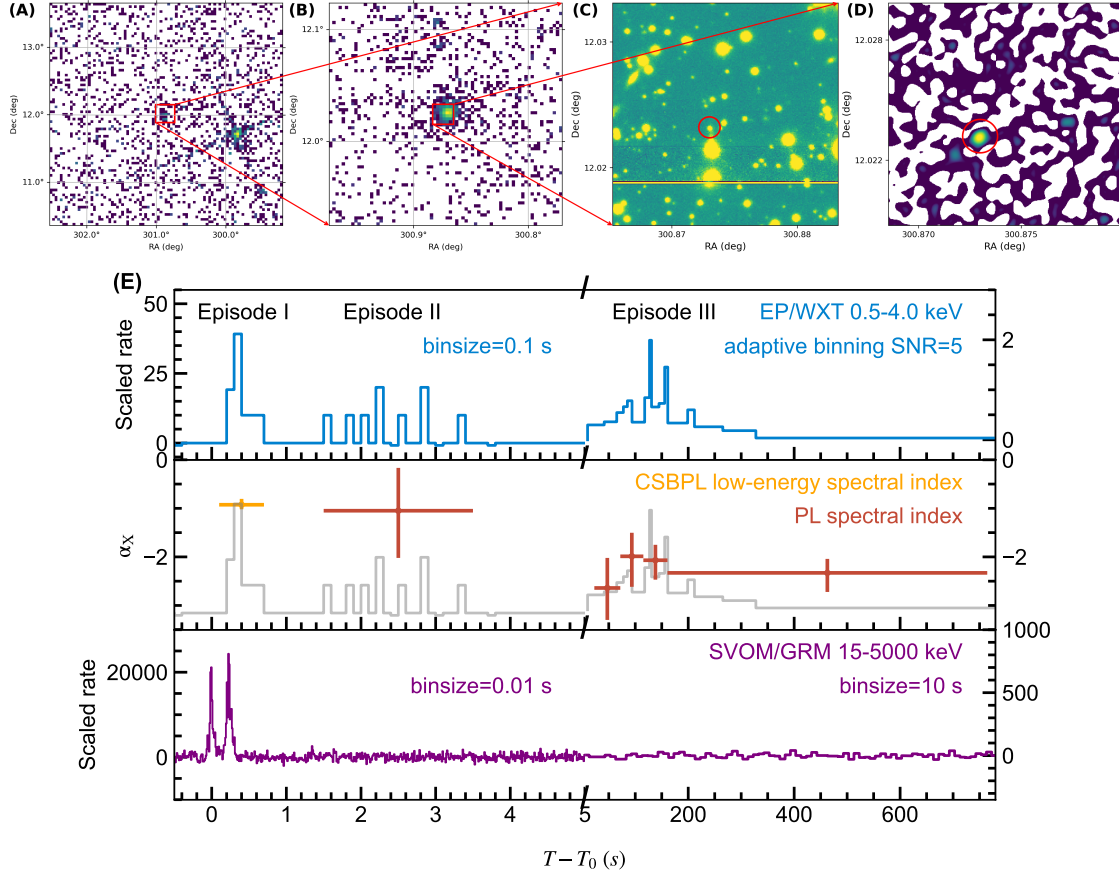


**Figure 1: Detection images and light curves for EP250704a/GRB 250704B in different bands.**

(A) The image generated from the clean event data of EP-WXT, the GRB source is recognized with the red box. (B) The image generated from the clean event data of EP-FXT, the GRB source is recognized with the red box. (C) The image from VLT captured by FORS2, the optical afterglow of the burst is highlighted in the red circle. (D) The image from VLA captured in 10 GHz, the radio afterglow of the burst is highlighted in the red circle. (E) The light curves and spectral evolution of EP250704a/GRB 250704B. The blue and grey curves show the light curves of EP250704a in the energy range of 0.5–4.0 keV. The purple curve represents the light curve of GRB 250704B in the energy range of 15–5000 keV. The yellow and red points denote the low-energy spectral indices derived from the best-fit parameters of PL and CSBPL models, respectively. All error bars on data points indicate their  $1\sigma$  confidence level.

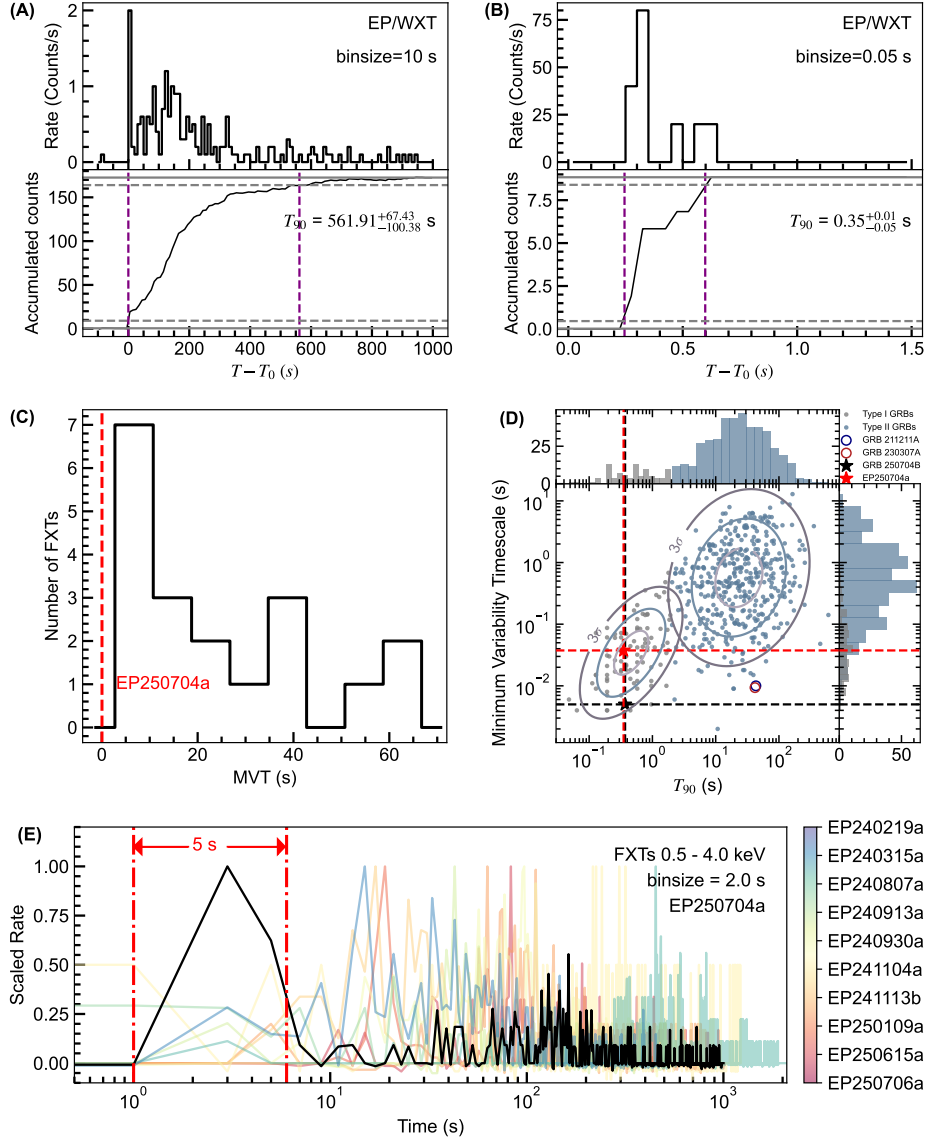


**Figure 2: Temporal and statistical analyses of EP250704a.** **(A)**  $T_{90}$  calculation of the EP/WXT detection of EP250704a. **(B)**  $T_{90}$  calculation of the initial spike of EP250704a detected by EP/WXT. In **(A)** and **(B)**, the black curves represent the light curve of EP/WXT in the energy range of 0.5–4 keV and the accumulated counts. The purple dashed vertical lines denote the  $T_{90}$  interval. The error bars mark the  $1\sigma$  confidence level. **(C)** Minimum variability timescale distribution of EP-detected FXTs. The red dashed vertical line denotes the location of EP250704a on the plot. **(D)** The minimum variability timescale versus  $T_{90}$  diagram. Type I and type II GRBs are represented by grey and cadet blue solid circles, respectively. EP250704a (Episode I) and GRB 250704B are highlighted by red and black stars, respectively. **(E)** The scaled light curves of the well-sampled EFXTs detected by EP during 1.5 years of operation, shown with the bin size of 2 s.

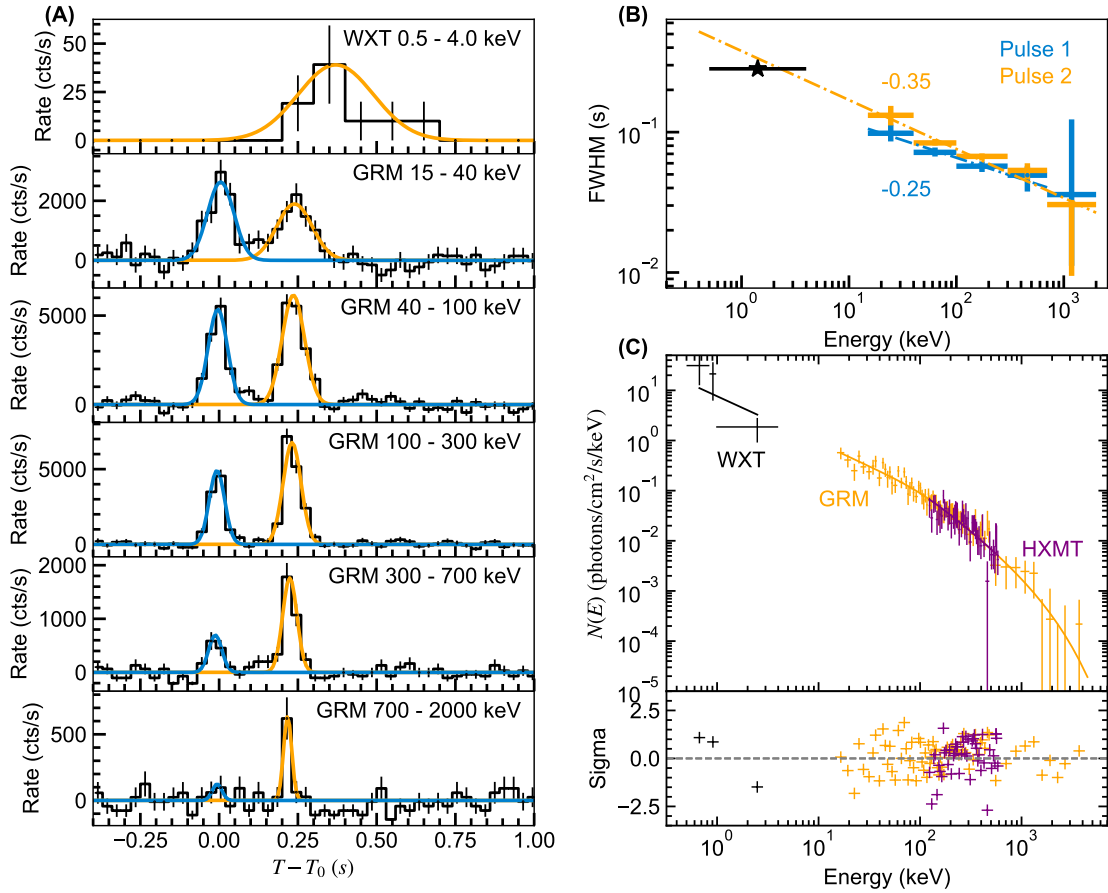


**Figure 3: Temporal and spectral consistency of the second pulse in the initial short spike. (A)** Multiwavelength light curves of EP250704a/GRB 250704B. The WXT light curve is binned at 0.1 s, and the GRM light curves at 0.03 s. The blue and yellow curves are the best-fit Gaussian models for GRM light curves and an empirical Gaussian profile for the WXT light curve, respectively. **(B)** The FWHMs derived from the Gaussian models as a function of energy. **(C)** The observed and modeled photon spectrum of the second pulse. All error bars mark the  $1\sigma$  confidence level.

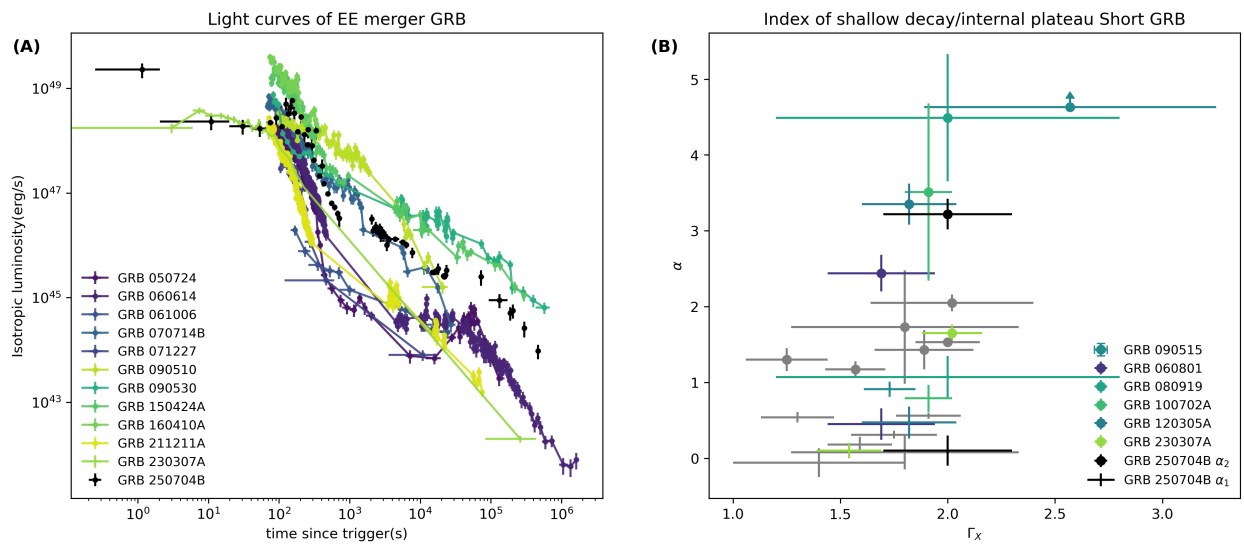


**Figure 4: Comparison between GRB 250704B and other short GRB afterglows.** (A) A comparison of the X-ray luminosity light curves between GRB 250704B and a sample of merger-type GRBs with extended emission (EE) observed by Swift. (B) Photon index  $\Gamma_X$  and decay-index comparison for the plateau phase ( $\alpha_1$ , small symbols) and the subsequent decay phase ( $\alpha_2$ , large symbols) for the sample of short GRBs with shallow decay. Grey dots show the normal shallow decay and colored dots show bursts with internal plateau.

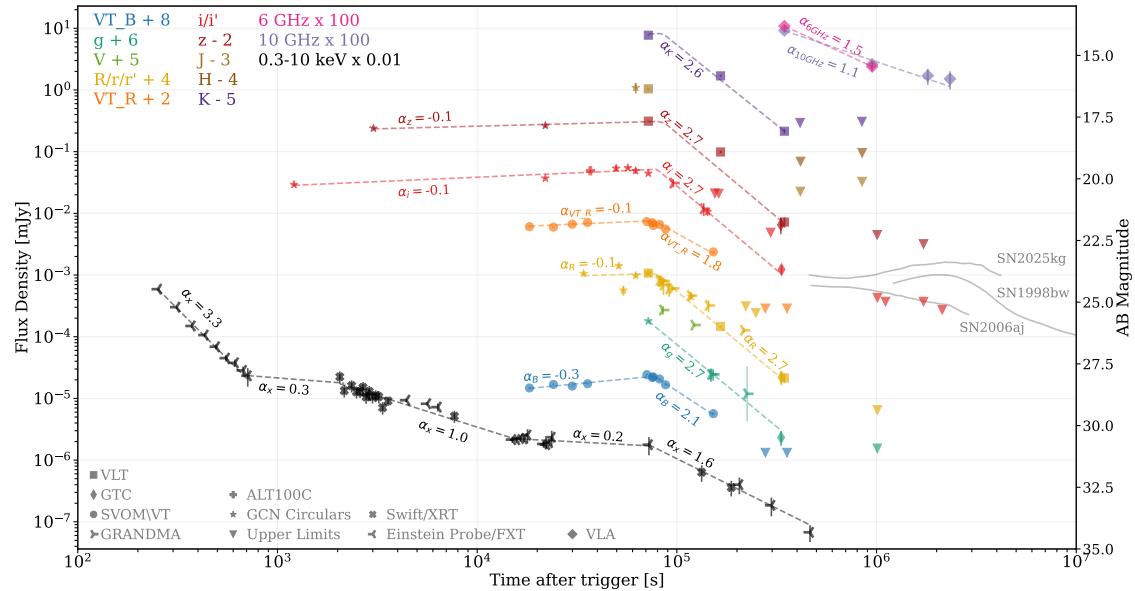


**Figure 5: Multi-band afterglow light curves of EP250704a/GRB 250704B.** Energy flux at different frequencies, from radio to X-rays, versus time since the GRB trigger. The temporal evolution can be described by multiple power-law segments (dashed lines). Error bars are at the  $1\sigma$  confidence level (c.l.). Downward triangles are upper limits at the  $3\sigma$  c.l. from VLT, SVOM/VT, GTC, OSN and GRANDMA. Observations are compared to the optical lightcurves of known GRB-SNe: SN2025kg (37), SN1998bw (38) and SN2006aj (39).

**Table 1: Observational properties.** All errors represent the  $1\sigma$  uncertainties.

Observed Properties	EP250704a/GRB 250704B
<b>Soft X-ray [0.5–4 keV]:</b>	
Total duration (s)	$561.91^{+67.43}_{-100.38}$
Spike duration (s)	$0.35^{+0.01}_{-0.05}$
EE spectral index $\alpha$	$-2.30 \pm 0.23$
EE flux ( $\text{erg cm}^{-2} \text{ s}^{-1}$ )	$2.16^{+0.22}_{-0.19} \times 10^{-10}$
EE fluence ( $\text{erg cm}^{-2}$ )	$1.61^{+0.16}_{-0.14} \times 10^{-7}$
EE luminosity ( $\text{erg s}^{-1}$ )	$2.61^{+0.27}_{-0.23} \times 10^{47}$
EE Isotropic energy (erg)	$1.93^{+0.20}_{-0.17} \times 10^{50}$
<b>Gamma-ray [10–1000 keV]:</b>	
Trigger time	2025-07-04 08:16:27.100
Duration (s)	$0.37 \pm 0.06$
Effective amplitude	$1.48 \pm 0.03$
Minimum variability timescale (ms)	5
Rest-frame spectral lag <sup>*</sup> (ms)	$2.5^{+3.5}_{-2.5}$
Spectral index $\alpha_1$	$-0.78^{+0.31}_{-0.27}$
Spectral index $\alpha_2$	$-1.46^{+0.22}_{-0.21}$
Break energy $E_b$ (keV)	$55.85^{+57.13}_{-26.47}$
Peak energy $E_p$ (keV)	$588.84^{+91.93}_{-122.18}$
Peak flux ( $\text{erg cm}^{-2} \text{ s}^{-1}$ )	$1.23^{+0.03}_{-0.03} \times 10^{-5}$
Total fluence ( $\text{erg cm}^{-2}$ )	$3.15^{+0.17}_{-0.21} \times 10^{-6}$
Peak luminosity ( $\text{erg s}^{-1}$ )	$1.80^{+0.06}_{-0.07} \times 10^{52}$
Isotropic energy (erg)	$3.79^{+0.20}_{-0.25} \times 10^{51}$
<b>Afterglow:</b>	
Redshift	$0.66102 \pm 0.00011$
<b>Associations:</b>	
Kilonova	Not detectable at $z=0.661$
Supernova	Ruled out: SN2025kg, SN1998bw, SN2006aj

<sup>\*</sup> The rest-frame spectral lag is measured between rest-frame energy bands 100–150 and 200–250 keV.

## References and Notes

1. D. Eichler, M. Livio, T. Piran, D. N. Schramm, Nucleosynthesis, neutrino bursts and  $\gamma$ -rays from coalescing neutron stars. *Nature* **340** (6229), 126–128 (1989), doi:10.1038/340126a0.
2. E. Berger, Short-Duration Gamma-Ray Bursts. *Annu. Rev. Astron. Astrophys.* **52**, 43–105 (2014), doi:10.1146/annurev-astro-081913-035926.
3. B. Zhang, *The Physics of Gamma-Ray Bursts* (Cambridge University Press) (2018), doi:10.1017/9781139226530.
4. Y.-H. I. Yin, *et al.*, Triggering the Untriggered: The First Einstein Probe-detected Gamma-Ray Burst 240219A and Its Implications. *Astrophys. J. Lett.* **975** (2), L27 (2024), doi:10.3847/2041-8213/ad8652.
5. Y. Liu, *et al.*, Soft X-ray prompt emission from the high-redshift gamma-ray burst EP240315a. *Nature Astronomy* **9**, 564–576 (2025), doi:10.1038/s41550-024-02449-8.
6. S.-Q. Jiang, *et al.*, EP240801a/XRF 240801B: An X-Ray Flash Detected by the Einstein Probe and the Implications of Its Multiband Afterglow. *Astrophys. J. Lett.* **988** (1), L34 (2025), doi:10.3847/2041-8213/addebf.
7. Y.-H. I. Yin, *et al.*, Spectral Hardening Reveals Afterglow Emergence in Long-duration Fast X-Ray Transients: A Case Study of GRB 250404A/EP250404a. *Astrophys. J. Lett.* **989** (2), L39 (2025), doi:10.3847/2041-8213/adf552.
8. Y. Q. Xue, *et al.*, A magnetar-powered X-ray transient as the aftermath of a binary neutron-star merger. *Nature* **568** (7751), 198–201 (2019), doi:10.1038/s41586-019-1079-5.
9. H. Sun, *et al.*, A Unified Binary Neutron Star Merger Magnetar Model for the Chandra X-Ray Transients CDF-S XT1 and XT2. *Astrophys. J.* **886** (2), 129 (2019), doi:10.3847/1538-4357/ab4bc7.
10. J. Quirola-Vásquez, *et al.*, New JWST redshifts for the host galaxies of CDF-S XT1 and XT2: Understanding their nature. *Astron. Astrophys.* **695**, A279 (2025), doi:10.1051/0004-6361/202451825.

11. J. S. Villasenor, *et al.*, Discovery of the short  $\gamma$ -ray burst GRB 050709. *Nature* **437** (7060), 855–858 (2005), doi:10.1038/nature04213.
12. W. Yuan, C. Zhang, Y. Chen, Z. Ling, The Einstein Probe Mission, in *Handbook of X-ray and Gamma-ray Astrophysics* (Springer Singapore), p. 86 (2022), doi:10.1007/978-981-16-4544-0\_151-1.
13. A. Li, *et al.*, EP250704a: Einstein Probe detection of an X-ray transient. *GRB Coordinates Network* **40941**, 1 (2025).
14. C.-W. Wang, *et al.*, GRB 250704B: SVOM/GRM observation of a short burst. *GRB Coordinates Network* **40940**, 1 (2025).
15. C.-W. Wang, S.-L. Xiong, C.-K. Li, C. Zheng, Insight-HXMT Team, GRB 250704B: Insight-HXMT detection. *GRB Coordinates Network* **40978**, 1 (2025).
16. D. Frederiks, *et al.*, Konus-Wind detection of short/hard GRB 250704B/ EP250704a. *GRB Coordinates Network* **40972**, 1 (2025).
17. A. Li, *et al.*, EP250704a: refined analysis of the EP-WXT and FXT follow-up observations. *GRB Coordinates Network* **40956**, 1 (2025).
18. L. Amati, The  $E_{p,i}$ - $E_{iso}$  correlation in gamma-ray bursts: updated observational status, re-analysis and main implications. *Mon. Not. R. Astron. Soc.* **372** (1), 233–245 (2006), doi:10.1111/j.1365-2966.2006.10840.x.
19. T. J. Galama, *et al.*, An unusual supernova in the error box of the  $\gamma$ -ray burst of 25 April 1998. *Nature* **395** (6703), 670–672 (1998), doi:10.1038/27150.
20. J. S. Bloom, *et al.*, The unusual afterglow of the  $\gamma$ -ray burst of 26 March 1998 as evidence for a supernova connection. *Nature* **401** (6752), 453–456 (1999), doi:10.1038/46744.
21. R.-F. Shen, B. Zhang, Prompt optical emission and synchrotron self-absorption constraints on emission site of GRBs. *Mon. Not. R. Astron. Soc.* **398** (4), 1936–1950 (2009), doi:10.1111/j.1365-2966.2009.15212.x.

22. B. Zhang, P. Mészáros, An Analysis of Gamma-Ray Burst Spectral Break Models. *Astrophys. J.* **581** (2), 1236–1247 (2002), doi:10.1086/344338.

23. B. Zhang, Early X-Ray and Optical Afterglow of Gravitational Wave Bursts from Mergers of Binary Neutron Stars. *Astrophys. J. Lett.* **763** (1), L22 (2013), doi:10.1088/2041-8205/763/1/L22.

24. D. N. Burrows, *et al.*, Bright X-ray Flares in Gamma-Ray Burst Afterglows. *Science* **309** (5742), 1833–1835 (2005), doi:10.1126/science.1116168.

25. B. Zhang, *et al.*, Physical Processes Shaping Gamma-Ray Burst X-Ray Afterglow Light Curves: Theoretical Implications from the Swift X-Ray Telescope Observations. *Astrophys. J.* **642** (1), 354–370 (2006), doi:10.1086/500723.

26. Y.-H. I. Yin, *et al.*, Spectral Hardening Reveals Afterglow Emergence in Long-duration Fast X-Ray Transients: A Case Study of GRB 250404A/EP250404a. *The Astrophysical Journal Letters* **989** (2), L39 (2025), doi:10.3847/2041-8213/adf552, <https://dx.doi.org/10.3847/2041-8213/adf552>.

27. H.-J. Lü, B. Zhang, W.-H. Lei, Y. Li, P. D. Lasky, The Millisecond Magnetar Central Engine in Short GRBs. *Astrophys. J.* **805** (2), 89 (2015), doi:10.1088/0004-637X/805/2/89.

28. J. P. Norris, J. T. Bonnell, Short Gamma-Ray Bursts with Extended Emission. *Astrophys. J.* **643** (1), 266–275 (2006), doi:10.1086/502796.

29. S. Dichiara, *et al.*, Evidence of Extended Emission in GRB 181123B and Other High-redshift Short GRBs. *Astrophys. J. Lett.* **911** (2), L28 (2021), doi:10.3847/2041-8213/abf562.

30. N. Gehrels, *et al.*, A new  $\gamma$ -ray burst classification scheme from GRB060614. *Nature* **444** (7122), 1044–1046 (2006), doi:10.1038/nature05376.

31. E. Troja, *et al.*, A nearby long gamma-ray burst from a merger of compact objects. *Nature* **612** (7939), 228–231 (2022), doi:10.1038/s41586-022-05327-3.

32. J. Yang, *et al.*, A long-duration gamma-ray burst with a peculiar origin. *Nature* **612** (7939), 232–235 (2022), doi:10.1038/s41586-022-05403-8.

33. H. Sun, *et al.*, Magnetar emergence in a peculiar gamma-ray burst from a compact star merger. *National Science Review* **12** (3), nwae401 (2025), doi:10.1093/nsr/nwae401.

34. A. Rowlinson, P. T. O'Brien, B. D. Metzger, N. R. Tanvir, A. J. Levan, Signatures of magnetar central engines in short GRB light curves. *Mon. Not. R. Astron. Soc.* **430** (2), 1061–1087 (2013), doi:10.1093/mnras/sts683.

35. S. D. Barthelmy, *et al.*, The Burst Alert Telescope (BAT) on the SWIFT Midex Mission. *Space Sci. Rev.* **120** (3-4), 143–164 (2005), doi:10.1007/s11214-005-5096-3.

36. B. O'Connor, *et al.*, A deep survey of short GRB host galaxies over  $z$  0-2: implications for offsets, redshifts, and environments. *Mon. Not. R. Astron. Soc.* **515** (4), 4890–4928 (2022), doi:10.1093/mnras/stac1982.

37. W. X. Li, *et al.*, An extremely soft and weak fast X-ray transient associated with a luminous supernova (2025), <https://arxiv.org/abs/2504.17034>.

38. A. Clocchiatti, *et al.*, THE ULTIMATE LIGHT CURVE OF SN 1998bw/GRB 980425. *The Astronomical Journal* **141** (5), 163 (2011), doi:10.1088/0004-6256/141/5/163, <http://dx.doi.org/10.1088/0004-6256/141/5/163>.

39. J. Sollerman, *et al.*, Supernova 2006aj and the associated X-Ray Flash 060218 . *Astronomy and Astrophysics* **454** (2), 503–509 (2006), doi:10.1051/0004-6361:20065226, <https://doi.org/10.1051/0004-6361:20065226>.

40. H. Cheng, *et al.*, Ground Calibration Result of the Wide-field X-ray Telescope (WXT) onboard the Einstein Probe. *arXiv e-prints* arXiv:2505.18939 (2025), doi:10.48550/arXiv.2505.18939.

41. Y. Dong, B. Wu, Y. Li, Y. Zhang, S. Zhang, SVOM gamma ray monitor. *Science China Physics, Mechanics, and Astronomy* **53**, 40–42 (2010), doi:10.1007/s11433-010-0011-7.

42. J. He, *et al.*, SVOM-GRM trigger performance study and verification. *Experimental Astronomy* **59** (1), 15 (2025), doi:10.1007/s10686-025-09983-x.

43. C.-W. Wang, *et al.*, BREAKFAST: A Framework for general joint BA duty and follow-up guidance of multiple  $\gamma$ -ray monitors (2025), <https://arxiv.org/abs/2510.15816>.

44. S. Zhang, *et al.*, The insight-HXMT mission and its recent progresses, in Space Telescopes and Instrumentation 2018: Ultraviolet to Gamma Ray, J.-W. A. den Herder, S. Nikzad, K. Nakazawa, Eds., vol. 10699 of Society of Photo-Optical Instrumentation Engineers (SPIE) Conference Series (2018), p. 106991U, doi:10.1117/12.2311835.

45. S.-N. Zhang, *et al.*, Overview to the Hard X-ray Modulation Telescope (Insight-HXMT) Satellite. Science China Physics, Mechanics, and Astronomy **63** (4), 249502 (2020), doi: 10.1007/s11433-019-1432-6.

46. X. Li, *et al.*, In-flight calibration of the Insight-Hard X-ray Modulation Telescope. Journal of High Energy Astrophysics **27**, 64–76 (2020), doi:10.1016/j.jheap.2020.02.009.

47. Q. Luo, *et al.*, Calibration of the instrumental response of Insight-HXMT/HE CsI detectors for gamma-ray monitoring. Journal of High Energy Astrophysics **27**, 1–13 (2020), doi:10.1016/j.jheap.2020.04.004.

48. C. Zheng, *et al.*, Improved Performance of Insight-HXMT/HE CsI detectors. Science China Physics, Mechanics, and Astronomy pp. – (2025), <https://www.sciengine.com/SCPMA/> doi/10.1007/s11433-025-2676-5.

49. D. Donato, *et al.*, The HEASARC Swift Gamma-Ray Burst Archive: The Pipeline and the Catalog. Astrophys. J. Suppl. Ser. **203** (1), 2 (2012), doi:10.1088/0067-0049/203/1/2.

50. P. A. Evans, *et al.*, An online repository of Swift/XRT light curves of  $\gamma$ -ray bursts. Astron. Astrophys. **469** (1), 379–385 (2007), doi:10.1051/0004-6361:20077530.

51. P. A. Evans, *et al.*, Methods and results of an automatic analysis of a complete sample of Swift-XRT observations of GRBs. Mon. Not. R. Astron. Soc. **397** (3), 1177–1201 (2009), doi: 10.1111/j.1365-2966.2009.14913.x.

52. I. Appenzeller, *et al.*, Successful commissioning of FORS1 - the first optical instrument on the VLT. The Messenger **94**, 1–6 (1998).

53. J. Wei, *et al.*, The Deep and Transient Universe in the SVOM Era: New Challenges and Opportunities - Scientific prospects of the SVOM mission. arXiv e-prints arXiv:1610.06892 (2016), doi:10.48550/arXiv.1610.06892.

54. S. Antier, *et al.*, GRANDMA observations of advanced LIGO's and advanced Virgo's third observational campaign. *Mon. Not. R. Astron. Soc.* **497** (4), 5518–5539 (2020), doi:10.1093/mnras/staa1846.

55. S. Karpov, STDweb: simple transient detection pipeline for the web. *Acta Polytechnica* **65** (1), 50–64 (2025), doi:10.14311/AP.2025.65.0050, <https://ojs.cvut.cz/ojs/index.php/ap/article/view/9969>.

56. H. Flewelling, Pan-STARRS Data Release 2, in *American Astronomical Society Meeting Abstracts #231*, vol. 231 of *American Astronomical Society Meeting Abstracts* (2018), p. 436.01.

57. H. Aihara, *et al.*, The Eighth Data Release of the Sloan Digital Sky Survey: First Data from SDSS-III. *Astrophys. J. Suppl. Ser.* **193** (2), 29 (2011), doi:10.1088/0067-0049/193/2/29.

58. A. Vallenari, *et al.*, Gaia Data Release 3: Summary of the content and survey properties. *Astronomy & Astrophysics* **674**, A1 (2023), doi:10.1051/0004-6361/202243940, <http://dx.doi.org/10.1051/0004-6361/202243940>.

59. K. C. Chambers, *et al.*, The Pan-STARRS1 Surveys (2019), <https://arxiv.org/abs/1612.05560>.

60. R. M. Cutri, *et al.*, 2MASS All Sky Catalog of point sources. (NASA/IPAC Infrared Science Archive) (2003).

61. E. F. Schlafly, D. P. Finkbeiner, Measuring Reddening with Sloan Digital Sky Survey Stellar Spectra and Recalibrating SFD. *The Astrophysical Journal* **737** (2), 103 (2011), doi:10.1088/0004-637X/737/2/103.

62. M. R. Blanton, *et al.*, New York University Value-Added Galaxy Catalog: A Galaxy Catalog Based on New Public Surveys. *Astron. J.* **129** (6), 2562–2578 (2005), doi:10.1086/429803.

63. J. J. Condon, *et al.*, The NRAO VLA Sky Survey. *Astron. J.* **115** (5), 1693–1716 (1998), doi:10.1086/300337.

64. CASA Team, *et al.*, CASA, the Common Astronomy Software Applications for Radio Astronomy. *Publ. Astron. Soc. Pac.* **134** (1041), 114501 (2022), doi:10.1088/1538-3873/ac9642.

65. K. A. Arnaud, XSPEC: The First Ten Years, in *Astronomical Data Analysis Software and Systems V*, G. H. Jacoby, J. Barnes, Eds., vol. 101 of *Astronomical Society of the Pacific Conference Series* (1996), p. 17.

66. G. Schwarz, Estimating the Dimension of a Model. *The Annals of Statistics* **6** (2), 461 – 464 (1978), doi:10.1214/aos/1176344136, <https://doi.org/10.1214/aos/1176344136>.

67. S. V. Golenetskii, E. P. Mazets, R. L. Aptekar, V. N. Ilinskii, Correlation between luminosity and temperature in  $\gamma$ -ray burst sources. *Nature* **306** (5942), 451–453 (1983), doi:10.1038/306451a0.

68. J. S. Bloom, S. R. Kulkarni, S. G. Djorgovski, The Observed Offset Distribution of Gamma-Ray Bursts from Their Host Galaxies: A Robust Clue to the Nature of the Progenitors. *Astron. J.* **123** (3), 1111–1148 (2002), doi:10.1086/338893.

69. J. Vernet, *et al.*, X-shooter, the new wide band intermediate resolution spectrograph at the ESO Very Large Telescope. *Astron. Astrophys.* **536**, A105 (2011), doi:10.1051/0004-6361/201117752.

70. W. Freudling, *et al.*, Automated data reduction workflows for astronomy. The ESO Reflex environment. *Astron. Astrophys.* **559**, A96 (2013), doi:10.1051/0004-6361/201322494.

71. J. An, *et al.*, EP250704a / GRB 250704B: VLT/X-shooter spectroscopic redshift  $z = 0.661$ . *GRB Coordinates Network* **40966**, 1 (2025).

72. R.-F. Shen, B. Zhang, Prompt optical emission and synchrotron self-absorption constraints on emission site of GRBs. *Mon. Not. R. Astron. Soc.* **398** (4), 1936–1950 (2009), doi:10.1111/j.1365-2966.2009.15212.x.

73. L. Amati, *et al.*, Intrinsic spectra and energetics of BeppoSAX Gamma-Ray Bursts with known redshifts. *Astron. Astrophys.* **390**, 81–89 (2002), doi:10.1051/0004-6361:20020722.

74. P. Y. Minaev, A. S. Pozanenko, The  $E_{p,I}$ - $E_{iso}$  correlation: type I gamma-ray bursts and the new classification method. *Mon. Not. R. Astron. Soc.* **492** (2), 1919–1936 (2020), doi:10.1093/mnras/stz3611.

75. D. Foreman-Mackey, D. W. Hogg, D. Lang, J. Goodman, emcee: The MCMC Hammer. *Publ. Astron. Soc. Pac.* **125** (925), 306 (2013), doi:10.1086/670067.

76. V. Z. Golkhou, N. R. Butler, O. M. Littlejohns, The Energy Dependence of GRB Minimum Variability Timescales. *Astrophys. J.* **811** (2), 93 (2015), doi:10.1088/0004-637X/811/2/93.

77. A. E. Camisasca, *et al.*, GRB minimum variability timescale with Insight-HXMT and Swift. Implications for progenitor models, dissipation physics, and GRB classifications. *Astron. Astrophys.* **671**, A112 (2023), doi:10.1051/0004-6361/202245657.

78. J. P. Norris, G. F. Marani, J. T. Bonnell, Connection between Energy-dependent Lags and Peak Luminosity in Gamma-Ray Bursts. *Astrophys. J.* **534** (1), 248–257 (2000), doi:10.1086/308725.

79. T. N. Ukwatta, *et al.*, The lag-luminosity relation in the GRB source frame: an investigation with Swift BAT bursts. *Mon. Not. R. Astron. Soc.* **419** (1), 614–623 (2012), doi:10.1111/j.1365-2966.2011.19723.x.

80. T. N. Ukwatta, *et al.*, Spectral Lags and the Lag-Luminosity Relation: An Investigation with Swift BAT Gamma-ray Bursts. *Astrophys. J.* **711** (2), 1073–1086 (2010), doi:10.1088/0004-637X/711/2/1073.

81. S. Xiao, *et al.*, A Robust Estimation of Lorentz Invariance Violation and Intrinsic Spectral Lag of Short Gamma-Ray Bursts. *Astrophys. J. Lett.* **924** (2), L29 (2022), doi:10.3847/2041-8213/ac478a.

82. H.-J. Lü, B. Zhang, E.-W. Liang, B.-B. Zhang, T. Sakamoto, The ‘amplitude’ parameter of gamma-ray bursts and its implications for GRB classification. *Mon. Not. R. Astron. Soc.* **442** (3), 1922–1929 (2014), doi:10.1093/mnras/stu982.

83. H.-J. Lü, E.-W. Liang, B.-B. Zhang, B. Zhang, A New Classification Method for Gamma-ray Bursts. *Astrophys. J.* **725** (2), 1965–1970 (2010), doi:10.1088/0004-637X/725/2/1965.

84. G. M. Green, dustmaps: A Python interface for maps of interstellar dust. *The Journal of Open Source Software* **3** (26), 695 (2018), doi:10.21105/joss.00695.

85. Y.-K. Chiang, Corrected SFD: A More Accurate Galactic Dust Map with Minimal Extragalactic Contamination. *Astrophys. J.* **958** (2), 118 (2023), doi:10.3847/1538-4357/acf4a1.

86. K. D. Gordon, *et al.*, One Relation for All Wavelengths: The Far-ultraviolet to Mid-infrared Milky Way Spectroscopic R(V)-dependent Dust Extinction Relationship. *Astrophys. J.* **950** (2), 86 (2023), doi:10.3847/1538-4357/accb59.

87. K. Gordon, dust\_extinction: Interstellar Dust Extinction Models. *The Journal of Open Source Software* **9** (100), 7023 (2024), doi:10.21105/joss.07023.

88. H. Gao, W.-H. Lei, Y.-C. Zou, X.-F. Wu, B. Zhang, A complete reference of the analytical synchrotron external shock models of gamma-ray bursts. *New Astron. Rev.* **57** (6), 141–190 (2013), doi:10.1016/j.newar.2013.10.001.

89. Z.-P. Zhu, *et al.*, Photometric and Spectroscopic Observations of GRB 190106A: Emission from Reverse and Forward Shocks with Late-time Energy Injection. *Astrophys. J.* **948** (1), 30 (2023), doi:10.3847/1538-4357/acbd96.

90. L. Zhao, *et al.*, The Shallow Decay Segment of GRB X-Ray Afterglow Revisited. *Astrophys. J.* **883** (1), 97 (2019), doi:10.3847/1538-4357/ab38c4.

91. C.-H. Tang, Y.-F. Huang, J.-J. Geng, Z.-B. Zhang, Statistical Study of Gamma-Ray Bursts with a Plateau Phase in the X-Ray Afterglow. *Astrophys. J. Suppl. Ser.* **245** (1), 1 (2019), doi:10.3847/1538-4365/ab4711.

## Acknowledgments

This work is based on the data obtained with Einstein Probe, a space mission supported by the Strategic Priority Program on Space Science of Chinese Academy of Sciences, in collaboration

with the European Space Agency, the Max-Planck-Institute for extraterrestrial Physics (Germany), and the Centre National d'Études Spatiales (France). We are grateful to the SVOM team for the development and operation of the SVOM mission. This work made use of data supplied by the UK Swift Science Data Centre at the University of Leicester. Based on observations collected at the European Organisation for Astronomical Research in the Southern Hemisphere under ESO programmes 114.27LW. AJCT wish to express his sincere thanks to W. H. Lee, D. Hiriart and all members of the San Pedro Mártir Observatory in México for their assistance and operations of the 0.6m Javier Gorosabel telescope at the BOOTES-5 station. GRANDMA thank A. Kaeouach, M. Masek, N. Sasaki, M. Lamoureux, T. Du Laz, S. Karpov, M. Freeberg, R. Hellot, K. Noysena, A. Klotz, Z. Benkhaldoun, G.M. Hamed, M.M. Elkhateeb, A.E. Abdelaziz, M. Molham, A. Takey, Y. Rajabov, T. Kvernadze, M. Coughlin, D. Turpin, N. Guessoum, P. Hello, P-A. Duverne, S. Karpov, T. Pradier for the core team.

**Funding:** The SVOM mission is supported by the Strategic Priority Research Program on Space Science of the Chinese Academy of Sciences. This work was supported by the National Natural Science Foundation of China (Grant Nos. 12573046, 12121003, to B.-B.Z.; 12273042, 12494572, to S.-L.X., C.-W.W., and W.-J.T.; 12573049 to H.S.; 12494571, 12494570, 12494573, 12133003, to L.-P.X.), the National Key Research and Development Programs of China (Grant Nos. 2022YFF0711404, 2022SKA0130102, to B.-B.Z.; 2021YFA0718500, to S.-L.X., C.-W.W; 2024YFA1611700, 2024YFA1611704, to L.-P.X.), the National SKA Program of China (Grant No. 2022SKA0130100, to B.-B.Z.), and the Strategic Priority Research Program of the Chinese Academy of Sciences (Grant Nos. XDA15360102, XDA15360300, XDB0550300, to S.-L.X., C.-W.W; XDB0550401, to L.-P.X.). B.-B.Z acknowledge support by the science research grants from the China Manned Space Program (CMS-CSST-2021-B11), the Fundamental Research Funds for the Central Universities, and the Program for Innovative Talents and Entrepreneurs in Jiangsu. AJCT acknowledges support from the Spanish Ministry project PID2023-151905OB-I00 and Junta de Andalucía grant P20\_010168 and from the Severo Ochoa grant CEX2021-001131-S funded by MCIN/AEI/ 10.13039/501100011033. OSN and GTC optical data were collected with the 1.5m telescope at the Observatorio de Sierra Nevada operated by the Instituto de Astrofísica de Andalucía, and by the 10.4m Gran Telescopio Canarias, installed at the Spanish Observatorio del

Roque de los Muchachos of the Instituto de Astrofísica de Canarias, on the island of La Palma. TRT data were based on observations made with the Thai Robotic Telescopes under program ID TRTC12B\_007, which is operated by the National Astronomical Research Institute of Thailand (Public Organization). AbAO team acknowledges Shota Rustaveli National Science Foundation of Georgia (SRNSFG). This work was supported by SRNSFG, grant FR-24-7713. NRIAG team acknowledges financial support from the Egyptian Science, Technology & Innovation Funding Authority (STDF) under grant number 45779. This research is based on observations made with the Thai Robotic Telescope under program ID TRTC12A\_001, which is operated by the National Astronomical Research Institute of Thailand (Public Organization). This article includes observations made in the Two-meter Twin Telescope (TTT) sited at the Teide Observatory of the Instituto de Astrofísica de Canarias (IAC), that Light Bridges operates on the island of Tenerife, Canary Islands (Spain). The Observing Time Rights (DTO) used for this research were provided by Light Bridges, SL. GRANDMA acknowledges the french PNHE (Programme National des Hautes Energies) support. BO is supported by the McWilliams Postdoctoral Fellowship in the McWilliams Center for Cosmology and Astrophysics at Carnegie Mellon University. E.T., N.P., Y.-H.Y., R.L.B. and R.R. were supported by the European Research Council through the Consolidator grant BHianca (grant agreement ID 101002761). DBM is funded by the European Union (ERC, HEAVYMETAL, 101071865). Views and opinions expressed are, however, those of the authors only and do not necessarily reflect those of the European Union or the European Research Council. Neither the European Union nor the granting authority can be held responsible for them. The Cosmic Dawn Center (DAWN) is funded by the Danish National Research Foundation under grant DNRF140. AS acknowledges support by a postdoctoral fellowship from the CNES. NRT acknowledges support from the UK STFC, grant ST/W000857/1.

**Author contributions:** B.-B.Z. and A.L. initiated the study. B.-B.Z., B.Z. coordinated the scientific investigations of the event. Y.-H.I.Y. analyzed the high energy prompt emission data. C.-W.W., S.-L.X., W.-J.T. and C.Z. contributed to the data analysis of SVOM/GRM and *Insight*/HXMT. J.-X.C. and X.-L.C. are the GRM burst advocates on July 4 2025. Y.-W.D., C.-K.L., X.-B.L., W.-J.T., C.-W.W., S.-L.X., S.-X.Y., S.-N.Z., C.Z. and S.-J.Z. contributed to the development and operation of SVOM/GRM and *Insight*/HXMT. L.-P.X. and H.-L.L processed the SVOM/VT data. A.L., Y.-H.C.,

C.Z., G.-Y.Z., Y.-J.Z. and W.-D.Z. are the WXT transient advocates on July 4 2025 and contributed to the discovery and preliminary analysis of the event. Y.L. H.S. and Q.-Y.W. contributed to the WXT data processing. Z.-X.L., C.Z. and W.-M.Y. contributed to the development of the WXT instrument. C. Z., Z.-X.L., H.-Q.C. and Y.L. contributed to the calibration of WXT data. Y.L., H.-Q.C., H.-W.P., D.-Y.L., J.-W.H., H.-Y.L. and H.S. contributed to the development of WXT data analysis software. Y.C. contributed to the development of the FXT instrument. S.-M.J. contributed to the development of FXT data analysis software. Y.-L.Q., J. W., X.-H.H., J.-Y.W. and C.B. contributed to the operation of VT. J.A., D.X., V.D.E., M.D.P., R.A.J.E.-F., D.H., A.J.L., D.B.M., D.P., A.S., N.R.T., S.D.V. contributed to the discovery and early characterization of the afterglow and provided feedback on the paper. M.G., S.B.P., R. S-R and A.J.C-T prepared GTC proposal and processed its data, R. S-R also analysis data from OSN. I.P.-G. analysis data from BOOTES-5/JGT. S.A., E.E., N.K., M.P., T.Y., M.T. and X.-F.W. contributed to the operation and data analysis of GRANDMA. E.T., R.B., N.P. and Y.-H.Y. led the VLT campaign and were responsible for data reduction and calibration. N.P. and Y.-H.Y. were responsible for the VLT X-shooter spectral analysis. B.O. and E.T. led the VLA campaign, R.R. was responsible for the radio data reduction and calibration. H.-J.L., H.G. provided idea about the EE, and A.L. search the Swift sample and made comparison. Y.-X.S. and Y.-D.H. made analysis to the late time optical observations. N.P., A.L., J.A., and D.X. made afterglow fitting and modeling process. A.L., Y.-H.I.Y., J.Y., W.-H.L., E.T., B.-B.Z., and B.Z. further investigated the physical model, completed the schematic diagram, and contributed to the discussion of the physical implications. B.-B.Z., E.T., Y.-H.I.Y., A.L. and B.Z. wrote the manuscript, with contributions from all authors.

**Competing interests:** There are no competing interests to declare.

**Data and materials availability:** The processed data are presented in the tables and figures of the paper, which are available upon reasonable request. Some data used in the paper are publicly available, whether through the UK Swift Science Data Centre website, or GCN circulars.

Upon reasonable requests, the code (mostly in Python) used to produce the results and figures will be provided.

## **Supplementary materials**

Materials and Methods

Figs. S1 to S5

Tables S1 to S4

References (40-91)

# Supplementary Materials for

## Minutes-long soft X-ray prompt emission from a compact object

### merger

An Li<sup>†</sup>, Chen-Wei Wang<sup>†</sup>, Niccolò Passaleva<sup>†</sup>, Jie An<sup>†</sup>,  
Bin-Bin Zhang\*, Eleonora Troja\*, Yi-Han Iris Yin\*,  
Yuan Liu, Shao-Lin Xiong, Li-Ping Xin, Yi-Xuan Shao, Jun Yang, Hui Sun,  
Dong Xu, Yu-Han Yang, Roberto Ricci, He Gao, Sarah Antier,  
Rosa L. Becerra, Jia-Xin Cao, Alberto Javier Castro-Tirado, Xin-Lei Chen,  
Ye-Hao Cheng, Yong Chen, Hua-Qing Cheng, Valerio D'Elia,  
Massimiliano De Pasquale, Yong-Wei Dong, Eslam Elhosseiny,  
Rob A. J. Eyles-Ferris, Maria Gritsevich, Xu-Hui Han, Dieter Hartmann,  
You-Dong Hu, Jing-Wei Hu\*, Shu-Mei Jia, Nino Kochiashvili,  
Wei-Hua Lei, Andrew J. Levan, Cheng-Kui Li, Dong-Yue Li, Hua-Li Li\*,  
Xiao-Bo Li, Zhi-Xing Ling, He-Yang Liu, Hou-Jun Lü, Daniele B. Malesani,  
Brendan O'Connor, Hai-Wu Pan, Shashi Bhushan Pandey, Ignacio Perez-Garcia,  
Daniëlle L. A. Pieterse, Marion Pillas, Yu-Lei Qiu, Andrea Saccardi,  
Rubén Sánchez-Ramírez, Wen-Jun Tan, Manasanun Tanasan, Nial R. Tanvir,  
Susanna D. Vergani, Jing Wang, Xiao-Feng Wang, Qin-Yu Wu, Shu-Xu Yi,  
Tillayev Yusufjon, Chen Zhang, Wen-Da Zhang, Yi-Jia Zhang, Guo-Ying Zhao,  
Chao Zheng, Shi-Jie Zheng, Chang Zhou, Ping Zhou, Bertrand Cordier,  
Jian-Yan Wei, Weimin Yuan, Shuang-Nan Zhang, Bing Zhang

\*Corresponding author. Email: B.-B. Z. (bbzhang@nju.edu.cn), E. T. (eleonora.troja@uniroma2.it), Y.-H. I. Y. (iris.yh.yin@connect.hku.hk), J.-W. H. (hujingwei@nao.cas.cn), H.-L. L. (lhl@nao.cas.cn)

<sup>†</sup>These authors contributed equally to this work.

**This PDF file includes:**

Materials and Methods

Figures S1 to S5

Tables S1 to S4

## Materials and Methods

### Observations and Data Reduction

**EP-WXT.** The Einstein Probe (EP), led by the Chinese Academy of Sciences (CAS) in collaboration with the European Space Agency (ESA) and the Max Planck Institute for extraterrestrial Physics (MPE), Germany, is a mission focused on the time-domain high-energy astrophysics. Among its two main payloads is Wide-field X-ray Telescope (WXT), which utilizes innovative lobster-eye micro-pore optics (MPO), enabling a large instantaneous field of view (FoV) of 3,600 square degrees and a sensitivity of  $\sim 2.6 \times 10^{-11} \text{ erg/cm}^2/\text{s}$  in 0.5–4 keV with 1 ks exposure. EP250704a was detected by the Wide-field X-ray Telescope (WXT) onboard the Einstein Probe (EP) during a monitoring target observation of 2RXS J210955.2+480922 from UTC 2025-07-04T07:49:30 to 2025-07-04T08:16:52 (ObsID: 11916650016). This source triggered the on-board processing unit 25 s after the Space Variable Objects Monitor (SVOM)/Gamma-ray Burst Monitor (GRM) trigger, and the autonomous EP-Follow-up X-ray Telescope (FXT) follow-up was preformed 221s after the WXT trigger. We recovered the WXT continued observation data during the slew phase. The WXT observation continued for  $\sim 800$  s after the trigger, and the burst emission before 334s was detected with a signal-to-noise ratio higher than  $3\sigma$ . The X-ray events data were selected and calibrated using the data reduction software and calibration database (CALDB) designed for WXT (Liu et al. in prep.). The CALDB is generated based on the results of the on-ground calibration experiments (40), the procedure of which has been applied to a prototype of WXT instrument. The image in the 0.5–4 keV range was extracted from the cleaned events (Fig. 1). The light curve and the spectrum of the source and background in a given time interval were extracted from a circle with a radius of 9 arcmin and an annulus with the radii of 18 arcmin and 36 arcmin, respectively.

**SVOM-GRM.** The Space-based multi-band astronomical Variable Objects Monitor (SVOM) mission is a Franco-Chinese mission dedicated to the study of GRB. It was launched on June 22, 2024. The Gamma-Ray Monitor (GRM) is one of its main instruments designed to measure the spectrum of high-energy bursts. GRM comprises three scintillator-based gamma-ray detectors (GRDs) operating in the 15 keV–5 MeV energy range onboard the Sino-French satellite SVOM (41, 42). On 2025-07-04T08:16:27.100 UTC (denoted as  $T_0$ ), all the three GRDs were triggered by a transient event with a signal-to-noise ratio of 29.6 in the 0.1-second time window. The real-time alert data

of this transient was downlinked to the ground through the VHF system with low latency, and then identified as a short burst GRB 250704B by the standard analysis process (43). Based on the preliminary result of VHF data, GRB 250704B was reported to the community by SVOM/GRM firstly (14). The event-by-event data, which is well calibrated (in preparation) in 15–5000 keV, is used for detailed temporal and spectral analysis.

**Insight-HXMT.** As China's first X-ray astronomy satellite, *Insight-HXMT* consists of three groups of collimated telescopes, namely the high energy X-ray telescope (HE), the medium energy X-ray telescope (ME) and the low energy X-ray telescope (LE) (44–46). GRB 250704B was detected by the CsI detectors of HE at  $T_0$ , which have a large effective area for gamma-ray photons penetrating the satellite platform (15). The energy range of CsI data used for spectral analysis is 120–600 keV, while for temporal analysis is 60–900 keV (47, 48). The data reduction follows the standard analysis process (43).

**EP-FXT.** The Follow-up X-ray Telescope (FXT) is one of the main payloads of EP in the 0.3–10 keV band, which offers three readout modes, i.e., Full Frame mode (FF), Partial Window mode (PW) and Timing mode (TM). The FXT is designed for quick follow-up observations and more precise positioning of transients, and for observations of targets of opportunity. EP-FXT carried out 6 follow-up observations of EP250704a/GRB 250704B, spanning from 221 seconds to approximately 5.4 days after the burst. The cumulative observation time exceeded  $5 \times 10^4$  s. During these observations, FXT-A observed in PW mode and FXT-B observed in FF mode in autonomous follow-up observation, both FXT-A and FXT-B observed in FF mode in later follow-up observations. All observations were conducted with a thin filter. The FXT data were processed using the FXT Data Analysis Software (FXTDAS v1.20), utilizing the latest FXT calibration database (CALDB v1.10). Source photons were extracted from a circle with a radius of 40 arcsec, while background photons were extracted from an annulus with the radii of 60 arcsec and 180 arcsec. FXT-B suffered from pile-up in FF mode for the first  $\sim 600$  s in the autonomous follow-up observation, during which time interval we only utilized the data from FXT-A in PW mode.

**Swift-XRT.** Swift-XRT has performed 4 follow up observations to EP250704a/GRB 250704B ranging from 2025-07-04T08:46:08 UTC to 2025-07-08T00:09:56 UTC with an exposure time of 11ks. All the observations were conducted in PC mode. The spectra and flux curves from XRT were selected by a circle source region with 30 pixel radius and an annuli background region with

80 to 120 pixel radius, and calibrated using the data reduction software in *HEASoft6.35.5* (49) package and the latest calibration database (CALDB) designed for XRT. To keep consistence with FXT observation, the flux curve were extracted within 0.5 to 10.0 keV energy range by *xrtgrblc* in *HEASoft* tools, same as the online tools result (50, 51).

**Optical and Near-Infrared imaging** We performed follow-up photometric observations with multiple instruments, including: ESO VLT UT1 (Antu) equipped with the FORS2 camera (52) under program 114.27LW (PI: E. Troja), ESO VLT UT4 (Yepun) equipped with the near-infrared HAWK-I imager under program 114.27LW (PI: E. Troja), 100-cm C telescope (ALT100C) of the JinShan project, located in Altay, Xinjiang, China, the 0.7-m telescope of the Thai Robotic Telescope network (TRT), located at Fresno, California, U.S.A (SRO), Visible telescope (VT) on board SVOM (53), 1.5 m telescope of Sierra Nevada Observatory (OSN, Granada, southern Spain, <http://www.osn.iaa.es/>), the 10.4m Gran Telescopio CANARIAS (GTC) equipped with the Optical System for Imaging and low-Intermediate-Resolution Integrated Spectroscopy (OSIRIS) instrument for optical bands and the Espectrógrafo Multiobjeto Infra-Rojo (EMIR) instrument for NIR bands, and the Global Rapid Advanced Network Devoted to the Multi-messenger Addict (GRANDMA (54)) contains kilonova-catcher telescopes (<http://kilonovacatcher.in2p3.fr/>), Ulugh Beg Astronomical Institute telescopes (UBAI NT-60 and UBAI AZT-22 at Maidanak Observatory), Kottamia Astronomical Observatory (KAO) telescopes, the ASO telescope at Oukaimeden Observatory and the Abastumani Astrophysical Observatory Telescope (AbAO-T150). Photometric results were derived using aperture photometry through standard procedures in the IRAF software. For GRANDMA results they were derived using the STDPipe pipeline and its web interface, to perform force photometry and template subtraction on a set of images obtained from different telescopes (55).

Photometric calibration in the *griz* bands was performed as follows. For VLT, TRT, and ALT100C observations, we used the Pan-STARRS DR2 catalog (56). The OSN observations were calibrated against field stars listed in the SDSS DR8 catalog (57). For instruments within the GRANDMA network, we used the Gaia DR3 catalog (58) for the *R*, *V*, and *I* bands, and the Pan-STARRS DR1 catalog (59) for the *g*, *r*, and *i* filters. SVOM/VT, VLT observations were directly calibrated in the AB magnitude system. For *BVRI* band photometry only, we adopted the transformation relations from <https://www.sdss4.org/dr12/algorithms/sdssUBVRITransform/>

\#Lupton2005. For the near-infrared(NIR) band they were corrected by 2MASS Point Source Catalog (60). The obtained photometric magnitudes in AB system and corrected for Galactic dust extinction, following the estimates of ref (61), are listed in Extended Data Table S3.

For GTC’s observations, due to high contamination from the wings of the point-spread function (PSF) of a nearby bright star, which affected background estimation at the position of GRB 250704B, PSF subtraction was performed prior to photometric analysis. We constructed an empirical PSF model using the `photutils.psf` routine, based on a set of unsaturated and isolated field stars. This model was used to fit and subtract the bright star near the GRB. A relationship between instrumental and absolute magnitudes was established by fitting the background-subtracted flux of these reference stars. This relation was then used to convert the background-subtracted flux of the target into absolute magnitudes. Finally, we applied the Vega-to-AB magnitude transformation (62) to report all results in the AB system, as provided in Extended Table S3.

**Radio.** We observed the source with the Karl G. Jansky Very Large Array (VLA) (63) in four X-band epochs at 10 GHz with 4 GHz bandwidth, under program 25A-309 (PI: Troja) and two C-band epochs at 6 GHz with 4 GHz bandwidth, under program SN078192 (PI: O’Connor). All data were obtained in the array configuration C, using 3C286 as the primary flux calibrator and J1950+0807 as the phase calibrator. Raw data were retrieved from the NRAO archive and processed with CASA v6.6.1 (64) using the standard VLA pipeline for flagging, bandpass, gain, and flux calibration. Imaging was performed with `tclean` adopting a Briggs weighting of 0.5 and Högbom deconvolution. The rms noise was measured in a source-free region, and a 5% calibration uncertainty was added in quadrature to the statistical error. Flux densities were determined from two-dimensional Gaussian fits, with the peak flux taken as the best estimate for point-like sources.

## Spectral Analysis

**Independent fit with gamma-ray spectra.** We conducted both time-integrated and time-resolved spectral analyses using gamma-ray data from SVOM/GRM (15–5000 keV) and Insight-HXMT (120–600 keV). The time intervals were determined according to individual pulses. The spectral fittings were carried out with the Python package, `bayspec`, following the methodology described in ref (26). The fittings were evaluated using PGSTAT (65), which is well suited for gamma-ray observations where the source spectrum follows Poisson statistics while the background spec-

trum is characterized by Gaussian errors. The spectral models adopted in the spectral fittings are summarized below:

- The power law (PL):

$$N(E) = A \left( \frac{E}{100 \text{ keV}} \right)^\alpha, \quad (\text{S1})$$

where  $A$  is the normalization parameter in units of photons  $\text{cm}^{-2} \text{ s}^{-1} \text{ keV}^{-1}$ , and  $\alpha$  is the spectral index at low energies.

- The cutoff power law (CPL):

$$N(E) = A \left( \frac{E}{100 \text{ keV}} \right)^\alpha \exp \left( -\frac{E}{E_c} \right), \quad (\text{S2})$$

where  $A$  is the normalization parameter,  $\alpha$  is the spectral index at low energies, and  $E_c$  is the cutoff energy in units of keV. The peak energy  $E_p = (2 + \alpha)E_c$ .

- The smoothly broken power law with high-energy exponential cutoff (CSBPL):

$$N(E) = AE_b^{\alpha_1} \left[ \left( \frac{E}{E_b} \right)^{-\alpha_1 n} + \left( \frac{E}{E_b} \right)^{-\alpha_2 n} \right]^{-\frac{1}{n}} \exp \left( -\frac{E}{E_c} \right), \quad (\text{S3})$$

where  $A$  is the normalization parameter,  $\alpha_1$  and  $\alpha_2$  are the spectral indices of the two smoothly-connected law segments at the break energy  $E_b$ . The smoothness parameter  $n$  is fixed to 5.38.  $E_p = (2 + \alpha_2)E_c$ .

We fitted the gamma-ray spectra with spectral models featured with high-energy exponential cutoffs, CPL and CSBPL, considering the limited instrumental coverage at the high-energy end. The models are compared based on the Bayesian Information Criterion (BIC) (66), and both provided comparable fits ( $\Delta \text{BIC} < 5$ ). The best-fit parameters and fitting statistics for each interval are listed in Extended Data Table S1, and the corresponding spectral parameter evolutions are presented in Extended Data Fig. S1.

**Independent fit with X-ray spectra.** We fitted the EP/WXT spectra with the absorbed PL model,  $tbabs*ztbabs*pl$ , adopting a Galactic absorption column density of  $N_{\text{H,gal}} = 8.94 \times 10^{20} \text{ cm}^{-2}$  and an intrinsic absorption column density of  $N_{\text{H,int}} = 6.52 \times 10^{21} \text{ cm}^{-2}$ , as determined from the EP/FXT spectral fittings with adequate statistical constraints (Methods). Time intervals are determined via adaptive rebinning of the light curve, requiring  $\geq 40$  background-subtracted net counts in each bin,

which are subsequently used for spectral fitting. Owing to the limited photon statistics, the WXT spectrum of the sharp spike does not provide meaningful constraints on the spectral shape and was thus analyzed through joint spectral fitting. The best-fit parameters and corresponding statistics for each time slice are listed in Extended Data Table S1. Based on the spectral fittings, we derived the spectral evolution, shown in Fig. 1. Generally, the spectral index follows an intensity-tracking pattern (67) up to  $\sim T_0 + 200$  s, with hard values of  $\alpha \sim -1$  in the initial spike and softer values of  $\alpha \sim -2$  in the long bump. A more resolved spectral evolution study was performed with EP/FXT data from  $T_0 + 222$  s onward, where the photon statistics are substantially improved.

**Joint fit with EP/WXT, SVOM/GRM and *Insight*-HXMT.** The joint fit of the second pulse, spanning  $T_0 + [0.1, 0.7]$  s, was carried out with both an absorbed CPL model  $tbabs*ztbabs*cpl$  and CSBPL model  $tbabs*ztbabs*csbpl$ . The absorption components were fixed to the values adopted in the independent fits of the X-ray prompt emission. The best-fit parameters and corresponding statistics are listed in Extended Data Table S2. The CPL parameters obtained from the independent fit to the gamma-ray spectrum in  $T_0 + [0.1, 0.4]$  s agree well with those from the joint fit, indicating that the spectral shape is primarily constrained by the gamma-ray data, which have higher photon statistics. Additionally, both CPL and CSBPL provide comparably good fits, with a BIC difference of less than 5. However, the CPL fitting shows residuals exceeding  $2\sigma$  in the X-ray band, whereas the CSBPL fitting keeps all deviations within  $2\sigma$ . Consequently, the joint analysis favors the CSBPL model for the spectrum of the second pulse.

**Spectral hardening transition in the long-duration X-ray detection with EP/FXT.** We conducted time-resolved spectral fitting of the EP/FXT data using the Python package *bayspec* (<https://github.com/jyangch/bayspec>), an upgraded version of *MySpecFit*, following the methodology outlined in ref (26). The time slices were divided by requiring a minimum of 200 accumulated photon counts to ensure adequate statistical significance in each time-resolved spectrum. Considering the brightness-induced pileup affecting FXT-B in full-frame mode, only FXT-A data were used for the spectral analysis within  $T_0 + [222, 717]$  s. For epochs later than  $T_0 + 3460$  s, joint spectral fittings were performed using spectra from both FXT-A and FXT-B. The goodness of fit was assessed by the reduced statistic  $STAT/dof$ , as described in ref (4), while model comparison employed the Bayesian information criterion (BIC) (66). The best-fit parameters and fitting statistics for each interval are listed in Extended Data Table S2, and the corresponding spectral index

evolution is presented in Extended Data Fig. S3.

The time-resolved spectral analysis reveals clear variable absorption across  $T_0+375.5$  s. Specifically, when fitting with the *tbabs*\**ztbabs*\**pl* model, the intrinsic absorption column density,  $N_{\text{H,int}}$ , was constrained to  $6.52_{-1.07}^{+1.17} \times 10^{21} \text{ cm}^{-2}$  during  $T_0+[222.0, 375.5]$  s, but declined to an unconstrained, negligible value afterward. Consequently, we adopted the model *tbabs*\**ztbabs*\**pl* with fixed intrinsic absorption column density  $N_{\text{H,int}} = 6.52 \times 10^{21} \text{ cm}^{-2}$  and galactic absorption column density  $N_{\text{H,gal}} = 8.94 \times 10^{20} \text{ cm}^{-2}$  for spectra prior to  $T_0+375.5$  s, and *tbabs*\**pl* with fixed  $N_{\text{H,gal}} = 8.94 \times 10^{20} \text{ cm}^{-2}$  for subsequent intervals.

The derived spectral indices,  $\alpha_X$ , exhibit a distinct soft–hard–flat spectral evolution pattern, which indicates the transition from the fading prompt emission to the emerging afterglow at around  $T_0+350$  s (26). The afterglow dominates the emission at later times from the observation starting at  $T_0+3460$  s, displaying a characteristic normal temporal decay expected for this phase.

**VLT/X-shooter Optical Spectroscopy.** EP250704a lies 13 arcsec away from a bright ( $r \sim 18$  AB mag) nearby ( $z = 0.1062$ ) galaxy, SDSS J200329.53+120109.9, which was initially considered as a possible host given its low chance-coincidence probability ( $P_{\text{cc}} \sim 2\%$ ) (68). To establish the source distance scale and its possible relation to the SDSS galaxy, spectroscopic observations were conducted with the X-shooter spectrograph (69) mounted on UT3 (Melipal) of ESO’s Very Large Telescope (VLT).

Here we utilize data from Programme 114.27LW (PI: E. Troja) and present the corresponding analysis and results. The observations consisted of  $4 \times 1200$  s exposures taken at an average airmass of 1.26 and seeing  $\sim 0.83$  arcsec. A slit width of 1.0 arcsec was used in the UVB arm and 0.9 arcsec in the other arms. Individual exposures were reduced using the official ESO Reflex pipeline (70) and then median combined into a single stacked spectrum. Superposed on a bright continuum, we identify multiple absorption lines due to Fe II, Mg I, and Mg II at a common redshift of  $z = 0.66102 \pm 0.00011$  (Extended Data Fig. S5), thereby ruling out the association with the nearby galaxy. This is consistent with the preliminary estimate reported in (71).

## Interpretation of spike consistency and divergence in Episodes I and II

**Gamma-ray first pulse without X-ray counterpart.** Based on the independent and joint spectral fitting results of the first and second pulses of GRB 250704B, we constructed the spectral energy

distributions (SEDs), illustrated in Extended Data Fig. S2. The single pulse detected in EP250704a is both temporally and spectrally consistent with the second pulse in GRB 250704B (Fig. 3), whereas no X-ray counterpart is associated with the first pulse. From the X-ray non-detection, we derived upper limits for the first pulse that fall below the extrapolation of the best-fit absorbed CPL model from the independent fit. This indicates a spectral break between the optical and X-ray bands, most likely attributable to the synchrotron self-absorption (72). By applying a broadband synchrotron spectrum for first pulse of GRB 250704B, with a low-energy spectral slope of  $f_\nu \propto \nu^2$ , we obtained a lower limit for the break energy of  $\nu_a \sim 6$  keV, resulting a theoretical flux just below the detection upper limits.

**Consistency of the second pulse in X-rays and gamma-rays.** The second pulse of the GRB 250704B spike, spanning  $T_0 + [0.1, 0.35]$  s, temporally overlaps with the single spike detected in EP250704a within  $T_0 + [0.2, 0.7]$  s. We modeled the second pulse with a Gaussian profile across different gamma-ray energy bands, revealing an anti-correlation between the full width at half maximum (FWHM) and energy. Confined by the limited photons in X-ray spike, we only described the pulse with a Gaussian model using morphologically reasonable parameters (Fig. 3). The resulting X-ray pulse width lies on the low-energy extrapolation of the second gamma-ray pulse, supporting their association. Spectrally, a joint fit of the WXT, GRM, and HXMT data over  $T_0 + [0.1, 0.7]$  s with an absorbed CSBPL model yields a good fit, consistent with a single emission component spanning from X-rays to gamma-rays. Notably, there is a peak time difference between the X-ray and gamma-ray pulses, a feature also seen in other associated EFXTs/GRBs (4, 26). The offset appears too large to be explained by conventional spectral lags and remains an open question in GRB prompt emission.

**X-ray tail lacking a gamma-ray counterpart.** Following the initial spike of Episode I, a decaying X-ray tail at  $\sim T_0 + [1.5, 3.5]$  s shows a consistently hard spectral index but without corresponding gamma-ray emission. This behavior aligns with the gradual flux decline from the second pulse of Episode I to Episode II. Assuming the same spectral shape as the second pulse of Episode I, the 15–5000 keV flux ( $\sim 1.44 \times 10^{-6}$  erg cm $^{-2}$  s $^{-1}$ ) is slightly below the SVOM/GRM sensitivity of  $\sim 2.37 \times 10^{-6}$  erg cm $^{-2}$  s $^{-1}$ .

## Statistical analysis

**Rest-frame peak energy ( $E_{\text{peak},z}$ )–isotropic gamma-ray energy ( $E_{\gamma,\text{iso}}$ ):** The  $E_{\text{peak},z}$ - $E_{\gamma,\text{iso}}$  relation, also named as Amati relation (73), is assumed to follow a linear form:

$$\log E_{\text{peak},z} = b + k \log E_{\gamma,\text{iso}}.$$

To derive the best-fitting values and their uncertainties based on previous GRB samples with known redshift (74), we use the MCMC method (75), which provides Bayesian posterior distributions for the model parameters. The results, with  $3\sigma$  uncertainties, are as follows: for Type I GRBs,  $k = 0.36_{-0.05}^{+0.04}$ ,  $b = -15.61_{-2.14}^{+2.51}$ ; for Type II GRBs,  $k = 0.39_{-0.02}^{+0.02}$ ,  $b = -17.82_{-0.98}^{+0.93}$ . The results for both Type I and Type II GRBs, including the fitted Amati relations and their associated  $3\sigma$  intrinsic scatter regions, are shown in Extended Data Fig. S4a. These findings provide a comprehensive characterization of the energy correlations in GRBs, which serves as a reference for the physical origin of GRB types.

**MVT-duration ( $T_{90}$ ):** The minimum variability timescale (MVT) is defined as the shortest timescale of significant variation that exceeds statistical noise in the GRB temporal profile. It serves as a probe of both the central engine’s activity and the geometric size of the emitting region (76, 77). The median rest-frame MVT (i.e., MVT/(1+z)) for type I and type II GRBs is 10 ms and 45 ms, respectively. To determine the MVT for GRB 250704B, we applied the Bayesian block algorithm to the full light curve in the GRM (15–1000 keV) and WXT (0.5–4 keV) bands, identifying the shortest block that encompasses the rising phase of a pulse. The MVT of GRB 250704B is approximately 5 ms in the gamma-ray band and about 37.5 ms in the X-ray band (Table 1). These values align more closely with the MVT distribution of type I GRBs (76) than with that of type II GRBs, as shown in Fig. 2d.

**Spectral lag–Peak luminosity:** Analysis shows that GRBs with shorter spectral lags generally exhibit higher peak luminosities (78, 79). Type I GRBs typically deviate from the main trend defined by Type II GRBs, showing systematically smaller spectral lags at comparable luminosities. This distinction makes the spectral lag–peak luminosity relation a useful tool for phenomenological classification. Using previously established samples of Type I and Type II GRBs with known redshifts (80, 81), we construct the  $L_{\gamma,\text{iso}}-\tau_z$  diagram, where  $L_{\gamma,\text{iso}}$  represents the isotropic peak luminosity and  $\tau_z = \tau/(1+z)$  is the rest-frame spectral lag. The relation for Type II GRBs is modeled

as  $\log L_{\gamma,\text{iso}} = b + k \log \tau_z$ . The best-fit parameters with  $1\sigma$  uncertainties are  $k = -0.94^{+0.07}_{-0.26}$ ,  $b = 54.24^{+0.49}_{-0.14}$ , and  $\log \sigma_{\text{int}} = -1.61^{+0.29}_{-0.17}$ . The best-fit relation and its  $3\sigma$  intrinsic scatter region are shown in Extended Data Fig. S4b. For GRB 250704B, the rest-frame spectral lag between the 100–150 keV and 200–250 keV energy bands is measured as  $\tau_z = 2.5^{+3.5}_{-2.5}$  ms. The corresponding isotropic peak luminosity, derived from SVOM-GRM spectral fitting and corrected for redshift, is  $L_{\gamma,\text{iso}} = (1.8^{+0.06}_{-0.07}) \times 10^{52}$  erg s $^{-1}$ . As illustrated in Extended Data Fig. S4(b), the position of GRB 250704B in this parameter space is clearly separated from the region occupied by Type II GRBs.

**Amplitude parameter ( $f_{\text{eff}}$ )-duration ( $T_{90}$ ):** The amplitude parameter is defined as  $f = F_p/F_b$ , in which  $F_p$  and  $F_b$  are the peak flux and background flux at the same epoch, respectively. To test whether a short-duration GRB is an intrinsically short type I GRB or is from a disguised short-duration GRB caused by the tip-of-iceberg effect (82), an effective amplitude parameter of long-duration GRB is defined as  $f_{\text{eff}} = F'_p/F_b$ . Here,  $F'_p$  is the simulated peak flux of prompt emission, which is rescaled down from the original long-duration GRB light curve until its signal above the background has a duration just shorter than 2 s. Following the calculation procedure presented in ref. (82), we obtain the effective amplitude as  $f_{\text{eff}} = 1.48 \pm 0.03$  for GRB 250704B in the gamma-ray band. It is consistent with the short-duration GRBs region in the  $f_{\text{eff}}-T_{90}$  diagram (Extended Data Fig.S4c), confirming the genuinely short-duration feature of the burst.

**$\epsilon$ -duration ( $T_{90}$ ):** A new phenomenological classification method for GRBs by adopting a new parameter  $\epsilon = E_{\gamma,\text{iso},52}/E_{\text{p,z},2}^{5/3}$  is proposed to identify the progenitor of GRBs (83), where  $E_{\gamma,\text{iso},52}$  is the isotropic gamma-ray energy in units of  $10^{52}$  erg, and  $E_{\text{p,z},2}$  is the cosmic rest-frame spectral peak energy in units of 100 keV. The  $\epsilon$  has a clear bimodal distribution (high- and low- $\epsilon$  regions) with a division line at  $\epsilon \sim 0.03$ , which corresponds to type I and type II GRB, respectively (83). We calculate the  $\epsilon$  for GRB 250704B, and then plot it in  $\epsilon - T_{90}$  diagram by comparing with other typical Type I and Type II GRBs which are taken from ref. (83) (Extended Data Fig.S4d). We obtain  $\epsilon \sim 0.008$  for GRB 250704B which falls into the low- $\epsilon$  region, suggesting that it is of a Type I origin.

## Afterglow Analysis

**X-ray and optical afterglows.** To investigate the physical processes in the afterglow, we corrected the afterglow flux using the *dustmaps* package (84). We adopted the Corrected SFD Reddening Map (CSFD) (85) to obtain the Galactic color excess  $E(B - V)$  along the line of sight. The optical photometry was then dereddened with the G23 extinction relation (86) implemented in the *dust\_extinction* (87) before being fitted to the afterglow model.

Empirically, we fitted the X-ray and optical afterglow light curves with multi-segment broken power-laws. For the X-ray light curve, the best model by Bayesian Information Criterion (BIC) is a broken power-law with four breaks. It exhibits (i) a steep decay ( $\alpha_1 = 3.3$ ) from  $T_0 + 2.5 \times 10^2$  s to  $6.9 \times 10^2$  s, (ii) a shallow decay ( $\alpha_2 = 0.3$ ) from  $6.9 \times 10^2$  s to  $2.1 \times 10^3$  s, (iii) a decay ( $\alpha_3 = 1.0$ ) from  $2.1 \times 10^3$  s to  $1.5 \times 10^4$  s, (iv) another shallow decay ( $\alpha_4 = 0.2$ ) from  $1.5 \times 10^4$  s to  $7.2 \times 10^4$  s, and finally (v) a normal decay ( $\alpha_5 = 1.6$ ) after  $7.2 \times 10^4$  s. The time-integrated spectra show no significant evolution in photon index or absorption. Time-resolved spectral analysis during the steep decay phase indicates that each segment is well fit by an absorbed power-law model (Extended Data Table S2). Assuming a common break time across all the optical and near-infrared bands, the light curves show two phases: (i) a slow rise ( $\alpha = 0.1$ ) during the early afterglow, coincident with the X-ray shallow decay, and (ii) after  $7.5 \times 10^4$  s a steep decay ( $\alpha = 2.7$ ). The discrepancy between the X-ray and optical light curves cannot be adequately explained by a standard afterglow model, suggesting the presence of energy injection. The simple decaying behavior, after  $7.5 \times 10^4$  s, is consistent with emission dominated by a normal forward shock.

To prove that the late-stage afterglow was dominated by the forward shock, we modeled the late-time ( $\geq 10^4$  s post-burst) light curve within the standard forward-shock framework. Based on the prompt-emission properties and the absence of a supernova-like component in the late-time optical afterglow, we adopted a uniform-density interstellar medium (ISM) and a viewing angle of  $0^\circ$  (on-axis). We modeled the forward-shock light curve with the numerical code PyFRS(<https://github.com/leihw/PyFRS>) (3, 88, 89), adopting a top-hat jet. Posterior distributions were obtained via Markov-chain Monte Carlo (MCMC) sampling implemented in the Python package *emcee* (75). We employed 70 walkers evolving for 20000 steps, setting the first 12000 steps as the burn-in phase. The resulting parameter constraints are listed in Extended Data Table S4. They show

reasonable jet opening angle and jet energy, which agree with those of normal type I bursts.

**Short GRBs X-ray afterglow comparison.** We compare the flux curve of EP250704a/GRB 250704B with the Swift GRB sample from February 2004 to July 2017. The EE and shallow decay GRB samples come from Swift observations. For the EE sample, we required a measured redshift, a recognizable EE component by the cumulative light curve, and at least two XRT orbits of afterglow data. Among 36 EE GRBs, 9 were selected and confirmed with previous papers. For the shallow decay sample, we followed earlier results from ref (90, 91) and included all 7 short GRBs listed there. We modeled the light curves of the shallow decay sample using powerlaw and broken powerlaw functions. Each powerlaw segment is described by a temporal decay index  $\alpha$ , defined through  $F(t) \propto t^{-\alpha}$ . A light curve was classified as exhibiting an internal plateau if it showed an initial nearly flat segment with temporal index  $\alpha_1$ , followed by a subsequent steep decay with temporal index  $\alpha_2$ . The steep decay was required to satisfy either  $\alpha_2 - \alpha_1 > 2$  or  $\alpha_2 > \Gamma_X + 1$  (91), where  $\Gamma_X$  is the photon index of the X-ray spectrum. Light curves that did not meet these criteria were classified as showing a normal shallow decay. In some cases such as GRB 250704B and GRB 230307A, the plateau feature appears at an early stage, beginning only a few hundred seconds after the burst trigger.

**Non-detection of supernova.** Deep multi-band imaging was carried out with the GTC 3 to 10 days after  $T_0$  and with VLT/FORS2 12 and 20 days after  $T_0$  in  $i$ -band. Here we compared the photometric upper limits obtained from these late time observations with the light curves of well studied and observed supernovae. We used the data of: SN2025kg (37), SN1998bw (38) and SN2006aj (39). We applied the cosmological correction, due to the expansion of the Universe, both to the time of observation, to go from rest to observer frame, and to the magnitudes, to account for the different distances of the afterglow and the supernovae emissions. The comparison reveals no evidence of an associated supernova (Fig. 5). Furthermore, empirical fitting of the late-time multi-band afterglow shows a simple power-law decay with an index of  $\sim 2$  and no signature of rebrightening, further supporting the lack of a supernova component.

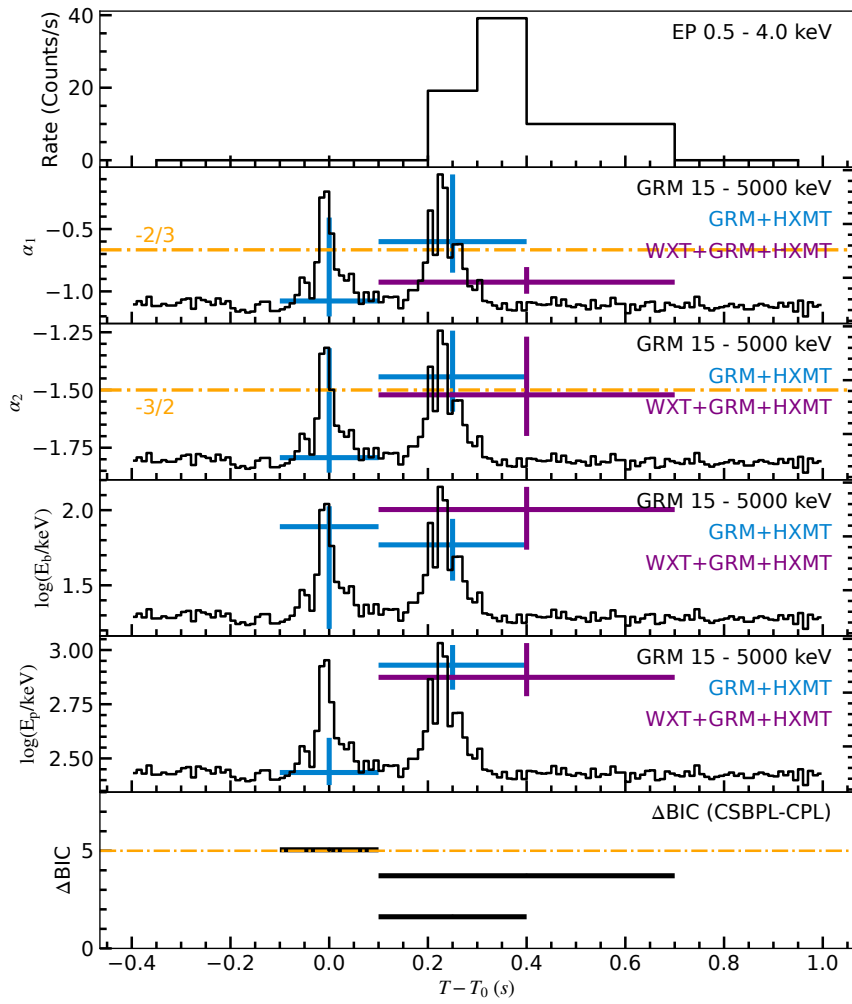


**Figure S1: Spectral evolution based on the best-fit parameters of CSBPL model and corresponding statistics.** The blue points represent the best-fit parameters derived from the joint GRM and HXMT fits, while the purple points are obtained from the joint GRM, HXMT and WXT fits. The bottom panel shows the BIC differences between the best-fit CSBPL and PL models. All error bars mark the  $1\sigma$  confidence level.

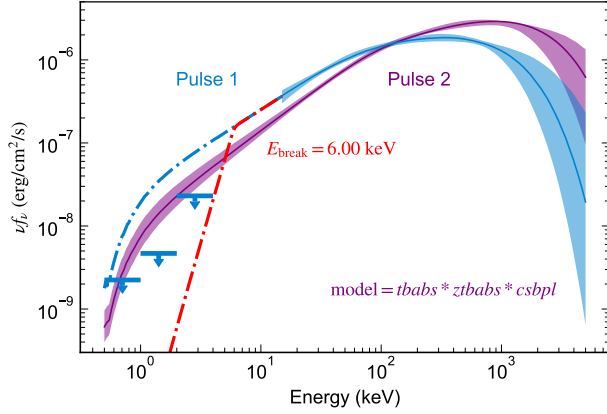


**Figure S2: SEDs of the first and second pulses in the initial spike.** The SEDs are obtained from the spectral fittings with the absorbed CSBPL model. The upper limits are constrained by the WXT non-detection of the first pulse. The synchrotron self-absorption break is fixed at 6.00 keV, and the low-energy spectral slope is fixed at 3.

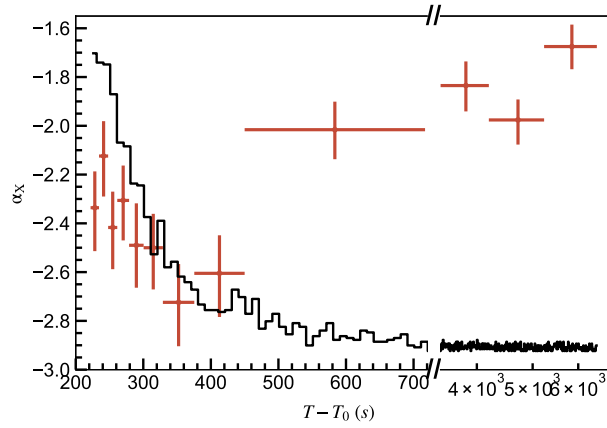


**Figure S3: The evolution of spectral index  $\alpha_X$ .** The red points represent the best-fit spectral indices in the time-resolved spectral fittings with fixed  $N_{\text{H}}$ . All error bars on data points represent their  $1\sigma$  confidence level.

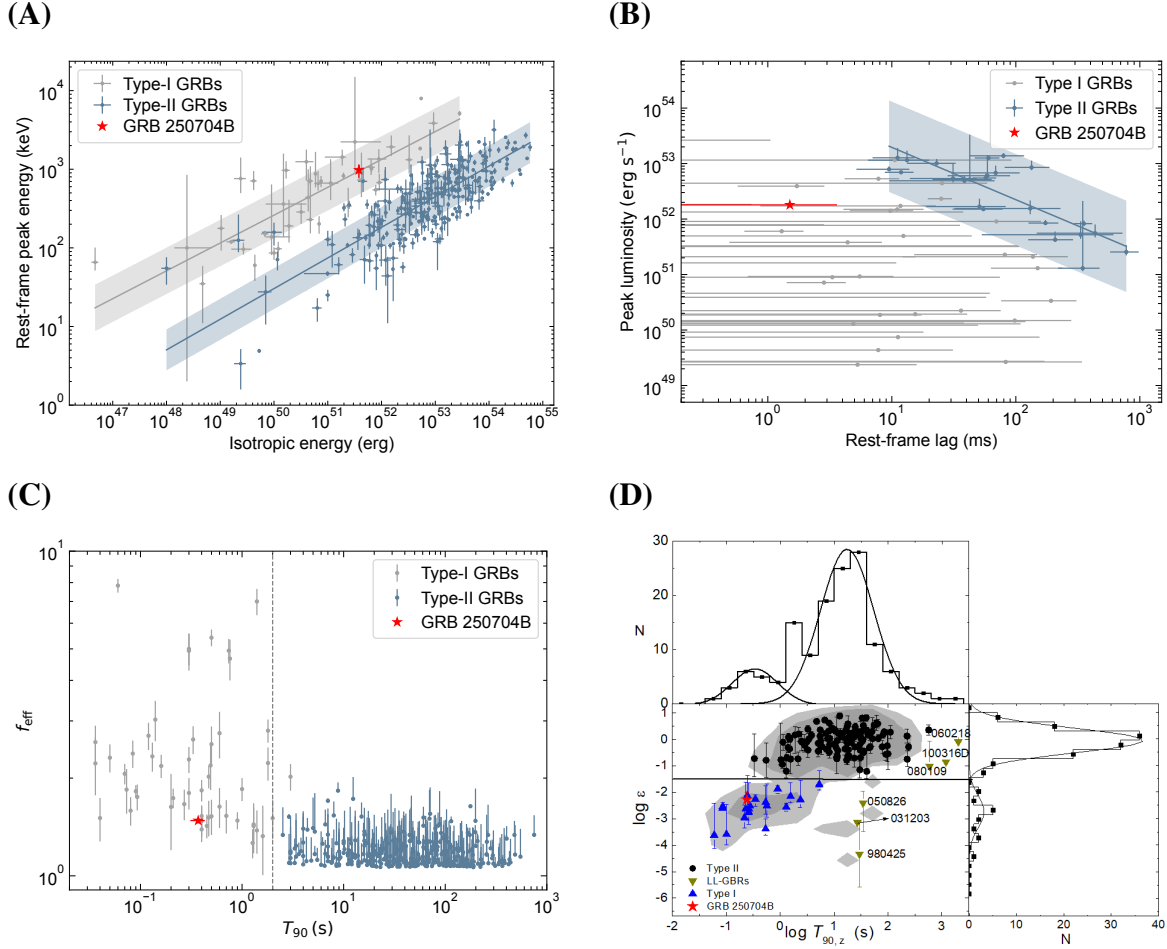


**Figure S4: The relationship of the observation properties from prompt emission of EP250704a/GRB 250704B.** (A) The Rest-frame peak energy versus  $T_{90}$  diagram (Amati relation). (B) The peak luminosity versus spectral lag diagram. (C) The  $f_{\text{eff}}$  versus  $T_{90}$  diagram. (D) The  $\epsilon$  versus  $T_{90}$  diagram. In (A–C), Type I and type II GRBs are represented by grey and cadet blue solid circles, respectively. In (D), Type I, type II and low luminosity GRBs are represented by blue triangles, black circles and green triangles, respectively. EP250704a/GRB 250704B is highlighted by red star in (A–D).

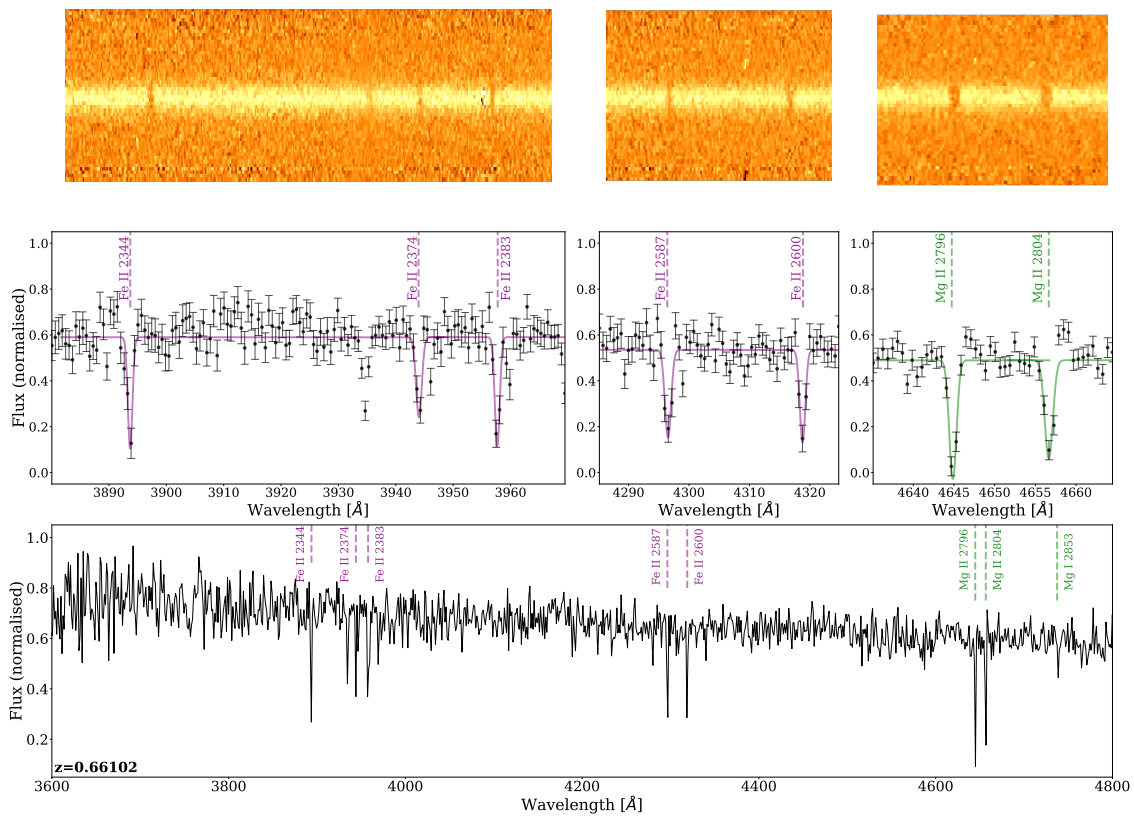


**Figure S5: Afterglow spectrum of EP250704a.** Multiple absorption lines at a common redshift of  $z=0.66102$  are imprinted on the afterglow light.

**Table S1:** Spectral fitting results and corresponding fitting statistics. All errors represent the  $1\sigma$  uncertainties.

t1 (s)	t2 (s)	$\alpha$	CPL model			CSBPL model							
			$E_p$ (photons $\text{cm}^{-2} \text{s}^{-1} \text{keV}^{-1}$ )	$\log A$ (photons $\text{cm}^{-2} \text{s}^{-1} \text{keV}^{-1}$ )	stat/dof <sup>f</sup>	$E_b$ (keV)	$E_p$ (keV)	$\alpha_1$	$\alpha_2$ (photons $\text{cm}^{-2} \text{s}^{-1} \text{keV}^{-1}$ )	stat/dof <sup>f</sup>	BIC		
-0.10	0.10	$-1.27^{+0.10}_{-0.09}$	$334.97^{+43.38}_{-35.16}$	$-0.96^{+0.04}_{-0.04}$	160.08/87	173.58	$77.62^{+23.54}_{-61.11}$	$272.27^{+421.28}_{-54.04}$	$-1.08^{+0.67}_{-0.67}$	$-1.79^{+0.47}_{-0.37}$	$1.28^{+0.21}_{-0.12}$	156.13/85	178.63
0.10	0.40	$-1.08^{+0.07}_{-0.08}$	$626.61^{+8.88}_{-9.07}$	$-1.04^{+0.03}_{-0.03}$	190.26/120	204.69	$58.75^{+23.75}_{-24.79}$	$851.14^{+303.25}_{-191.99}$	$-0.60^{+0.34}_{-0.25}$	$-1.44^{+0.20}_{-0.15}$	$0.38^{+0.39}_{-0.39}$	182.25/118	206.31
-0.10	0.40	$-1.13^{+0.06}_{-0.06}$	$489.78^{+5.24}_{-5.34}$	$-0.99^{+0.02}_{-0.03}$	163.85/128	178.48	$55.85^{+57.13}_{-26.17}$	$588.84^{+91.93}_{-22.18}$	$-0.78^{+0.31}_{-0.27}$	$-1.46^{+0.22}_{-0.21}$	$0.75^{+0.40}_{-0.31}$	156.73/126	181.11
0.10	0.70	$-1.05^{+0.06}_{-0.05}$	$613.76^{+59.21}_{-59.14}$	$-1.04^{+0.03}_{-0.03}$	194.83/123	209.34	$100.93^{+41.96}_{-46.35}$	$748.17^{+328.40}_{-35.82}$	$-0.93^{+0.12}_{-0.09}$	$-1.52^{+0.45}_{-0.48}$	$0.88^{+0.15}_{-0.18}$	188.88/121	213.06

**Table S2:** Spectral fitting results and corresponding fitting statistics for EP/WXT and EP/FXT. All errors represent the  $1\sigma$  uncertainties.

$t1$ (s)	$t2$ (s)	PL Model			
		$\alpha_X$	log A (photons $\text{cm}^{-2} \text{s}^{-1} \text{keV}^{-1}$ )	pgstat/dof	BIC
1.50	3.50	$-1.05^{+0.88}_{-0.97}$	$-1.80^{+1.61}_{-1.85}$	0.19/1	2.39
22.76	71.77	$-2.64^{+0.62}_{-0.66}$	$-5.83^{+1.22}_{-1.36}$	4.28/4	7.87
71.77	115.29	$-1.99^{+0.49}_{-0.63}$	$-4.45^{+0.92}_{-1.26}$	5.87/3	9.08
115.29	160.80	$-2.07^{+0.32}_{-0.40}$	$-4.64^{+0.62}_{-0.78}$	12.28/10	17.25
160.80	764.50	$-2.33^{+0.29}_{-0.39}$	$-6.08^{+0.56}_{-0.78}$	11.11/16	16.89
22.76	764.50	$-2.30^{+0.23}_{-0.23}$	$-5.75^{+0.46}_{-0.46}$	174.26/39	181.68
222.00	234.50	$-2.34^{+0.15}_{-0.18}$	$-5.65^{+0.28}_{-0.34}$	58.83/57	66.98
234.50	248.00	$-2.12^{+0.14}_{-0.17}$	$-5.29^{+0.27}_{-0.31}$	49.25/58	57.43
248.00	261.50	$-2.42^{+0.15}_{-0.17}$	$-5.86^{+0.28}_{-0.32}$	51.46/56	59.58
261.50	279.00	$-2.31^{+0.14}_{-0.16}$	$-5.75^{+0.26}_{-0.30}$	40.87/55	48.96
279.00	300.50	$-2.49^{+0.17}_{-0.17}$	$-6.21^{+0.33}_{-0.34}$	45.98/56	54.1
300.50	329.00	$-2.50^{+0.14}_{-0.17}$	$-6.34^{+0.25}_{-0.33}$	62.13/56	70.25
329.00	375.50	$-2.72^{+0.16}_{-0.18}$	$-6.97^{+0.30}_{-0.35}$	49.12/56	57.25
375.50	450.00	$-2.60^{+0.16}_{-0.18}$	$-7.12^{+0.30}_{-0.36}$	68.94/55	77.03
450.00	717.00	$-2.02^{+0.11}_{-0.12}$	$-6.36^{+0.21}_{-0.24}$	65.42/78	74.18
3460.00	4196.50	$-1.83^{+0.10}_{-0.11}$	$-6.67^{+0.18}_{-0.20}$	122.06/107	131.44
4196.50	5234.50	$-1.98^{+0.08}_{-0.10}$	$-7.00^{+0.16}_{-0.20}$	129.85/126	139.55
5234.50	6464.00	$-1.68^{+0.09}_{-0.09}$	$-6.45^{+0.17}_{-0.18}$	151.30/145	161.28

**Table S3:** Optical and Radio Afterglow Observations of GRB 250704B/EP250704a

Optical					
Time (days)	Observatory	Band	Magnitude <sup>*</sup>	Error	Reference
0.014	COLIBRI	i	20.24	0.20	GCN 40942
0.035	VLT/FORS2	z	19.95	0.02	GCN 40945
0.260	Pan-STARRS	i	19.98	0.03	GCN 40958
0.260	Pan-STARRS	z	19.84	0.07	GCN 40958
0.395	GROWTH-India	r	19.84	0.08	GCN 40962
0.575	GROWTH-India	i	19.58	0.09	GCN 40962
0.592	GROWTH-India	r	19.53	0.09	GCN 40962
0.625	SAO	R	20.68	0.18	GCN 40963
0.658	NOT	i	19.56	0.05	GCN 40971
0.720	FTW	i	19.68	0.10	GCN 40974
0.720	FTW	J	19.31	0.20	GCN 40974
0.720	FTW	r	19.92	0.10	GCN 40974
0.833	GSP	g	19.76	0.20	GCN 40975
0.833	GSP	i	19.78	0.20	GCN 40975
0.833	GSP	r	19.82	0.20	GCN 40975
0.439	NOWT	V	19.60	0.16	GCN 40999
1.367	Mondy-AZT-33IK	R	20.78	0.05	GCN 41024
1.648	NOT	i	21.34	0.14	GCN 40993
0.833	VLT/HAWK-I	J	19.36	0.01	This work
0.833	VLT/HAWK-I	Ks	19.18	0.01	This work
0.833	VLT/FORS2	r	19.82	0.01	This work
0.833	VLT/FORS2	z	19.66	0.01	This work
1.917	VLT/HAWK-I	Ks	20.83	0.03	This work
1.917	VLT/FORS2	r	21.98	0.02	This work
1.917	VLT/FORS2	z	20.91	0.04	This work

next

Time (days)	Observatory	Band	Magnitude <sup>*</sup>	Error	Reference
3.970	VLT/HAWK-I	Ks	23.07	0.09	This work
3.970	VLT/FORS2	r	24.07	0.18	This work
3.970	VLT/FORS2	z	23.75	0.19	This work
12.830	VLT/FORS2	i	>24.98	-	This work
19.896	VLT/FORS2	i	>24.98	-	This work
19.896	VLT/FORS2	z	>24.64	-	This work
0.212	SVOM/VT	VT-B	20.48	0.01	This work
0.212	SVOM/VT	VT-R	19.94	0.01	This work
0.279	SVOM/VT	VT-B	20.33	0.01	This work
0.279	SVOM/VT	VT-R	19.96	0.01	This work
0.346	SVOM/VT	VT-B	20.40	0.01	This work
0.346	SVOM/VT	VT-R	19.84	0.01	This work
0.414	SVOM/VT	VT-B	20.30	0.01	This work
0.414	SVOM/VT	VT-R	19.77	0.01	This work
0.819	SVOM/VT	VT-B	19.94	0.01	This work
0.819	SVOM/VT	VT-R	19.73	0.01	This work
0.873	SVOM/VT	VT-B	20.05	0.03	This work
0.873	SVOM/VT	VT-R	19.78	0.02	This work
0.882	SVOM/VT	VT-B	20.03	0.02	This work
0.882	SVOM/VT	VT-R	19.89	0.02	This work
0.948	SVOM/VT	VT-B	20.11	0.01	This work
0.948	SVOM/VT	VT-R	19.85	0.01	This work
1.016	SVOM/VT	VT-B	20.35	0.02	This work
1.016	SVOM/VT	VT-R	20.04	0.01	This work
1.763	SVOM/VT	VT-B	21.52	0.02	This work
1.763	SVOM/VT	VT-R	20.96	0.02	This work
3.211	SVOM/VT	VT-B	>23.10	-	This work
3.211	SVOM/VT	VT-R	>23.25	-	This work

next

Time (days)	Observatory	Band	Magnitude <sup>*</sup>	Error	Reference
4.122	SVOM/VT	VT-B	>23.10	-	This work
4.122	SVOM/VT	VT-R	>23.25	-	This work
3.838	GTC	z	23.86	0.30	This work
3.851	GTC	g	24.48	0.27	This work
3.862	GTC	r	24.04	0.26	This work
3.868	GTC	i	23.68	0.17	This work
4.794	GTC	Ks	>22.73	-	This work
4.808	GTC	J	>23.52	-	This work
4.816	GTC	H	>23.30	-	This work
9.778	GTC	Ks	>22.68	-	This work
9.793	GTC	J	>23.12	-	This work
9.802	GTC	H	>22.95	-	This work
11.658	GTC	z	>24.27	-	This work
11.671	GTC	g	>24.92	-	This work
11.681	GTC	r	>25.37	-	This work
11.688	GTC	i	>24.82	-	This work
24.682	GTC	i	>25.31	-	This work
0.427	ALT100C	i	19.68	0.05	This work
1.795	OSN	i	>20.59	-	This work
0.947	KNC	r	20.11	0.22	This work
0.970	KNC	r	20.13	0.15	This work
0.991	KNC	r	20.13	0.12	This work
0.992	KNC	r	20.29	0.32	This work
1.060	KNC	r	20.44	0.26	This work
1.670	KNC	r	21.12	0.23	This work
1.715	KNC	g	21.94	0.24	This work
1.761	KNC	g	21.93	0.22	This work
2.564	KNC	r	>21.15	-	This work

next

Time (days)	Observatory	Band	Magnitude <sup>*</sup>	Error	Reference
2.604	KNC	g	22.72	1.12	This work
0.986	TRT-SRO	V	20.32	0.16	This work
1.107	TRT-SRO	r	20.42	0.09	This work
1.111	TRT-SRO	I	20.20	0.15	This work
1.875	TRT-SRO	I	>20.62	-	This work
2.878	TRT-SRO	r	>21.42	-	This work
1.358	UBAI/NT-60	r	20.72	0.52	This work
1.416	UBAI/AZT-22	V	20.93	0.05	This work
2.507	UBAI/AZT-22	r	22.12	0.20	This work
1.578	KAO	i	21.22	0.24	This work
3.412	AbAO-T150	i	>22.18	-	This work

Radio					
Time (days)	Observatory	Band	Flux [ $\mu$ Jy]	Error [ $\mu$ Jy]	Reference
3.950	VLA	6 GHz	109	8	This work
3.950	VLA	10 GHz	92	7	This work
10.890	VLA	6 GHz	24	6	This work
10.890	VLA	10 GHz	26	4	This work
19.880	VLA	10 GHz	17	5	This work
26.820	VLA	10 GHz	15	5	This work

<sup>\*</sup> All magnitude in this table were corrected by galactic absorption described in Method and reported in the AB system.

**Table S4:** Distributions of MCMC-Fitted Parameters with PyFRS.

Parameter	Unit	Prior Type	Parameter Bound	Posterior Value
$\log_{10}(E_{k,\text{iso}})$	erg	log – uniform	[51, 55]	$52.62_{-0.09}^{+0.08}$
$\log_{10}(\Gamma_0)$	1	log – uniform	[1, 3]	$1.51_{-0.06}^{+0.05}$
$\log_{10}(n_{18})$	$\text{cm}^{-3}$	log – uniform	[-4, 0]	$-2.96_{-0.34}^{+0.41}$
$\theta_j$	degree	uniform	[0, 15]	$3.08_{-0.34}^{+0.48}$
$p$	1	uniform	[2.01, 2.9]	$2.39_{-0.01}^{+0.01}$
$\log_{10}(\epsilon_e)$	1	log – uniform	[-3, 0]	$-0.82_{-0.07}^{+0.09}$
$\log_{10}(\epsilon_B)$	1	log – uniform	[-5, -0.3]	$-1.06_{-0.24}^{+0.19}$